Modeling ice shelf cavities and calving tabular icebergs

A.A. Stern,[1] , A. Adcroft[1] and O. Sergienko[1] , G. Marquez[1], R. Hallberg[1]

3 **Key Points:**

4

A. A. Stern, Geophysical Fluid Dynamics Laboratory, Princeton University

A. Adcroft, Geophysical Fluid Dynamics Laboratory, Princeton University

O. Sergienko, Geophysical Fluid Dynamics Laboratory, Princeton University

G. Marquez, Geophysical Fluid Dynamics Laboratory, Princeton University

R. Hallberg, Geophysical Fluid Dynamics Laboratory, Princeton University

Abstract.   The calving of giant icebergs is an important process in the

Antarctic freshwater cycle. Iceberg calving can significantly alter the geom-

etry of an ice shelf cavity, potentially affecting the circulation within the cav-

ity. Furthermore, giant icebergs which break away can drift across large dis-

tance, altering ocean circulation, sea ice distributions and bottom water for-

mation. However the despite its importance, the current generation of nu-

merical models is unable to represent this process in a physically realistic way.

In this study we develop a model of an ice shelf cavity using a Lagrangian

ice shelf. The ice shelf is constructed out of Lagrangian elements which are

bonded together by numerical bonds. This Lagrangian framework allows for

large pieces of the ice shelf to break away and become tabular icebergs. The

model developed in the manuscript is referred to as the Lagrangian Iceberg/Ice

Shelf Model (LIISM). This paper provides a description of the LIISM model

and discusses a number of the technical elements involved in building a La-

grangian ice shelf. To test the model, the LIISM is used to model an ideal-

ized ice shelf cavity which was developed as part of the Marine Ice Ocean

Modeling Inter-comparison Project (MISOMIP). Results from static ice shelf

experiments compare well to results using a more traditional Eularian ice

shelf cavity. The novel capabilities of the LIISM are demonstrated by mod-

eling a tabular iceberg breaking away from the idealized ice shelf.

1. Introduction

Floating ice shelves cover vast regions of the Antarctic polar oceans. These massive platforms of ice extend deep into the water column, applying large pressures to surface of the ocean, which is often hundreds of meters below global sea level. Beneath the ice shelves, both the bottom topography and the ice shelf geometry play a role in steering ocean currents [Nicholls , 1996; Jenkins et al , 2010; Stern et al , 2014]. The topographic constraint imposed by the ice shelf at the ocean's upper boundary significantly affects the circulation within the ice shelf cavities, and gives the ocean within the ice shelves cavities a unique character.

In addition to suppressing the depth of ocean surface, the ice shelves also melt (and break), thus providing a freshwater flux into the ice shelf cavities. Ice shelf melting and breaking are key components in the Antarctic meltwater system, and affect the ocean hydrography and biology both inside and outside of the ice shelf cavities. Some elements of the this Antarctic meltwater system are discussed in the following paragraphs.

Within the ice shelf cavities, the input of buoyant meltwater into the ocean creates rising density plumes, which are guided along the ice shelf base, and help drive ocean circulation beneath the ice shelves [MacAyeal , 1984; Holland and Feltham , 2006]. The strength of the circulation within the cavity feeds back onto the ice shelf melt rates, by removing cold water from the cavity, and drawing in warmer waters from the open ocean, thus providing the constant supply of thermal energy needed for continuous ice shelf melt [Lewis and Perkin , 1986; Jacobs et al , 2011].

45   The Antarctic ice shelves are also characterized by large infrequent calving events where

46   massive pieces of the ice shelves break off, to create giant tabular icebergs. Observational

47   estimates suggest that approximately half of Antarctic ice shelf decay is due to iceberg

48   calving, while the other half occurs through ice shelf melting [Depoorter et al , 2013;

49   Rignot et al , 2013]. Calving icebergs' sizes appear to fit a power law distribution, with

50   the majority of icebergs being small (L< 1 km), while giant tabular icebergs (L > 5km)

51   account for more than 90% of the icebergs mass [Tournadre et al , 2016]. After calving,

52   icebergs slowly drift away from their mother glaciers, often becoming stuck in sea ice, or

53   become grounded along the Antarctic coast [Lichey and Hellmer , 2001; Dowdeswell and

54   Bamber , 2007]. Giant tabular icebergs also extend deep into the water column, and have

55   to potential to disrupt ocean circulation patterns for months or even years after calving

56   [Robinson et al , 2012; Stern et al , 2015].

57   Melt water from both ice shelf melt and iceberg melt impact the ocean hydrography

58   outside of the ice shelf cavities, influencing sea ice production and bottom water formation

59   [Arrigo et al , 2002; Robinson et al , 2012; Nicholls et al , 2009]. The long distances traveled

60   by giant icebergs before melting means that their meltwater impact is often felt hundreds

61   of kilometers away from their calving origins [Stern et al , 2016]. Melt water injection (and

62   the accompanying upwelling) from ice shelves and icebergs can also influence biological

63   productivity by providing nutrients to the surface ocean or changing sea ice conditions

64   [Arrigo et al , 2002; Vernet et al , 2012; Biddle et al , 2015]. The increased productivity

65   associated with free floating tabular icebergs has been linked with local increases in ocean

66   carbon uptake, potentially large enough to be a significant fraction of the Southern Ocean

67   carbon sequestration [Smith et al , 2007].

68   In recent years society's need for improved projections of future sea level has lead to an

69   increased focus on the Antarctic meltwater system described in the previous paragraphs.

70   This increased interest has led to accelerated efforts to accurately model Antarctic ice shelf

71   cavities [Asay-Davis et al , 2016]. Modeling the ocean beneath the ice shelves presents

72   a unique set of challenges, since (i) the presence of ice shelves provides a rigid upper

73   boundary for the ocean model which is not encountered elsewhere in the ocean, and

74   (ii) melting and breaking ice shelves imply a changing ocean boundary conditions which

75   present numerous numerical difficulties.

76   The earliest models of ocean ice shelf cavities were developed using a static ice shelf

77   with a fixed shape [Hellmer and Olbers , 1989; Determan and Gerdes , 1994; Grosfeld et

78   al , 1997; Holland and Jenkins , 2001; Losch , 2008]. In these models, ice shelf melting

79   was represented through salinity and temperature fluxes, while the ice shelf geometry

80   remained unchanged. Later models of ice shelf cavities allowed the ice shelf geometry

81   to evolve as the ice shelf melted, permitting the study of coupled ocean-ice phenomena

82   [Gladish et al , 2012; Sergienko , 2013]. More recently, dynamic ice shelf models have

83   been coupled the ocean cavity, allowing the study of grounding line migration, which is of

84   key importance for sea level rise projections [Grosfeld and Sandhger , 2004; Goldberg et

85   al , 2012; De Rydt and Gudmundsson , 2016]. As far as we know, all models of ice shelf

86   cavities to date have neglected ice shelf breaking and iceberg detachment.

87   In parallel to these efforts to develop ice shelf cavity models, a number of iceberg drift

88   models have been developed, and have been included in some global General Circulation

89   Models [Bigg et al , 1997; Gladstone et al , 2001; Martin and Adcroft , 2010; Marsh et al ,

90   2015]. These iceberg drift models treat icebergs as Lagrangian point particles, which are

advected by the flow, and melt according to certain parameterizations for icebergs melt. Since icebergs are treated as point particles, the iceberg drift models are mostly suitable for modeling smaller icebergs drifting across large distances, and as such iceberg drift models have mostly been used to represent icebergs smaller than 3.5km on a global scale [Jongma et al , 2009; Martin and Adcroft , 2010; Marsh et al , 2015]. These models are not suitable for modeling larger tabular icebergs, which feel the ocean over many grid cells, depress the ocean surface and change circulation patterns [Stern et al , 2016]. They also not suitable for studying the local effects that icebergs have on the surrounding ocean. For this reason, tabular icebergs (L > 5km) are currently not represented in the iceberg drift models used in climate models, even though observations suggest that tabular icebergs account for the vast majority of the total Southern Hemisphere icebergs mass [Tournadre et al , 2016].

The ice shelf cavity models and iceberg drift models described above have been developed separately from one another, and have not been designed to be used together in a physically consistent way. As such, it has not been possible to model the calving of tabular icebergs away from an ice shelf, which is an important part of the Antarctic climate system. The goal of this study is to develop a model which combines features of the ice shelf cavity models and the iceberg drift models, to create an ice shelf cavity model that is able to calve tabular icebergs. To do this, we create an ice shelf model out of Lagrangian elements which are 'bonded' together by numerical bonds. In this framework, icebergs do not get created when a calving event takes place (as in iceberg drift models), but rather the icebergs 'break' away from an existing ice shelf, thus changing the geometry of the ice shelf cavity. Modeling iceberg calving in a physically consistent way allows us to study the

114 ocean response to iceberg detachment (see Figures 1 and Figures 2, for example). Also, by

115 allowing icebergs protrude deep into the water column we can study the ocean dynamics

116 around individual tabular icebergs (which was not possible in iceberg drift models).

117 In all simulation in this study, the shape of the calving iceberg is prescribed. The

118 question of how to correctly prescribe a calving law is undoubtably a very important

119 question, which has rightfully received much attention in recent years [Benn et all , 2007;

120 Alley et al , 2008; Levermann et al , 2012]. Bassis and Jacobs [2013], for example, used

121 a DEM model to study the generation and propagation of cracks within an ice shelf (not

122 coupled to a dynamic ocean model). In this study, we bypass the question of how to

123 correctly calve icebergs or break bonds. Instead we focus on developing a framework to

124 model the ocean to response to ice shelf breaking and the presence of tabular icebergs.

125 This framework of representing ice shelves using a Lagrangian grid might be a step towards

126 including giant tabular icebergs in climate models. Including ice fracture into this model

127 will be a later step.

128 The model developed in this study is referred to at the Lagrangian Iceberg/Ice Shelf

129 Model (LIISM). Section 2 gives a description of many of the key aspects of the LIISM.

130 Since this model is a new approach to modeling ice shelf cavities, we present many of

131 the technical elements involved in constructing the model. Those readers who are more

132 interested in the model capabilities, should skip directly to the model results in the later

133 sections. In Section 3 and 4, the LIISM model is used to simulate the circulation beneath

134 an idealized ice shelf. The LIISM model results are validated by comparing them to an

135 existing ice shelf model. We then we move beyond the capabilities of the existing ice shelf

136 model by allowing a piece of the ice shelf to break away becoming a tabular icebergs, and

137 consider the ocean response to this calving event.

2. Model description

138 In this section we describe many key elements of the LIISM. The LIISM is a

139 Lagrangian/particle-based model in that the objects of the model are Lagrangian ele-

140 ments. Each element represents a mass of ice which is floating in the ocean, and has a

141 position, velocity, mass, and a set of dimensions, which can evolve in time. The motion of

142 each element is determined by a momentum equation which is solved in the (Lagrangian)

143 reference frame of the element. The elements are forced by oceanic and atmospheric

144 forces, which are provided by the user or are determined by coupling the LIISM to an

145 ocean/atmosphere model. The elements also interact with one another and can be bonded

146 together to form larger structures. In different contexts, the LIISM elements can be

147 thought to represent individual icebergs, sea ice flows, or, when the elements are bonded

148 together, they can represent larger structures such as tabular icebergs or ice shelves. In

149 this latter case, the LIISM model can be categorized as a discrete element model (DEM).

150 The LIISM model is developed on the code base of an existing iceberg drift model

151 [Martin and Adcroft , 2010; Stern et al , 2016]. When run with the correct set of runtime

152 flags, the model runs as a traditional iceberg drift model.

2.1. Equations of motion

153 The elements drift in the ocean, forced by atmosphere, ocean and sea-ice drag forces,

154 as well as the Coriolis force and a force due to the sea surface slope. When these ice

155 elements move alone (without interactions with other elements), they can be thought of

156 as representation of small icebergs, and follow the same equations described in the iceberg

157 drift model of Martin and Adcroft [2010] (based on the equations outlined in Bigg et al

158 [1997]; Gladstone et al [2001]).

159 In addition to the environmental forces, the elements in the LIISM model experience

160 interactive forces due to the presence of other elements. Two types of interactive forces are

161 included between elements. The first force is repulsive force which is applied to elements

162 to prevent them from moving too close to one another. This repulsive force prevents

163 icebergs from piling up on top of one another. The second interactive force is a force due

164 to numerical 'bonds', and is only applied if two elements are 'bonded' together. When

165 two elements are bonded, each element feels an attractive force that prevents the elements

166 from moving too far apart from one another. The interactive forces between two bonded

167 elements are defined such that in the absence of other forces the elements come to rest

168 adjacent to one another, with no overlap of the iceberg areas.

The momentum equation for each element is given by

$$M\frac{D\vec{u}}{Dt} = \vec{F}_A + \vec{F}_W + \vec{F}_R + \vec{F}_C + \vec{F}_{SS} + \vec{F}_{SI} + \vec{F}_{IA}, \tag{1}$$

169 where $\frac{D}{Dt}$ is the total (Lagrangian) derivative, M is the mass of the element, $\vec{u}$ is the

170 velocity of the element, and the terms on the right hand side give the forces on the

171 element due to air drag ($\vec{F}_A$), water drag ($\vec{F}_W$), sea ice drag ($\vec{F}_{SI}$), Coriolis force ($\vec{F}_C$),

172 wave radiation force ($\vec{F}_R$), sea surface slope ($\vec{F}_{SS}$), and interactions with other elements

173 ($\vec{F}_{IA}$). The environmental forces are the same as those presented in Martin and Adcroft

174 [2010], and are provided for completeness in Appendix A. The details of the interactive

175 forces are provided in below.

2.2. Interactive Forces

The interactive force on an element is calculated by adding together the interactions with all other elements, such that the interactive force on element i, $(\vec{F}_{IA})_i$ is given by:

$$(F_{IA})_i = \Sigma_{j \neq i}(F_{IA})_{ij}, \tag{2}$$

where $(F_{IA})_{ij}$ is the force on element i by element j. Both bonded an repulsive interactions are modeled using elastic stresses with frictional damping. The elastic component of the force is a function of the distance between the two elements, while the frictional damping force depends on the relative velocity of the two elements.

To describe the forces between two elements, we begin by introducing some notation. Let $\vec{x}_i$, $\vec{x}_j$ be the positions of elements i and j. The distance between elements i and j is

$$d_{ij} = |\vec{x}_i - \vec{x}_j|. \tag{3}$$

We then define the interaction diameter of an element by

$$D_i = 2\sqrt{\frac{A_i}{\pi}}, \tag{4}$$

where A_i is the planar surface area of element i. Using this, we define the critical interactive length scale,

$$L_{ij} = \frac{D_i + D_j}{2}, \tag{5}$$

which governs interactions between elements i and j. Repulsive forces are only applied when $d_{i,j} < L_{i,j}$, while bonded forces are only applied when the when $d_{i,j} > L_{i,j}$ and a bond exists between element i and j. Bond and repulsive forces are designed to such that in the absence of other forces, bonded particles will settle in an equilibrium position where elements are separated by the critical interaction length scale $L_{i,j}$.

To aid in notation, we define a bond matrix B_{ij} such that $B_{ij} = 1$ if elements i and j are bonded together and $B_{ij} = 0$ otherwise. Using this notation, the interactive force $(\vec{F_{IA}})_{ij}$ on an element i by an element j is given by

$$(\vec{F_{IA}})_{ij} = \begin{cases} (\vec{F_e})_{ij} + (\vec{F_d})_{ij} & \text{if } d_{ij} \leq L_{ij} \\ (\vec{F_e})_{ij} + (\vec{F_d})_{ij} & \text{if } d_{ij} > L_{ij} \text{ and } B_{ij} = 1 \\ 0 & \text{if } d_{ij} > L_{ij} \text{ and } B_{ij} = 0 \,. \end{cases} \tag{6}$$

$(\vec{F_e})_{ij}$ and $(\vec{F_d})_{ij}$ are the elastic and frictional damping components of the interactive force between elements i and j. The elastic force $(\vec{F_e})_{ij}$ between elements is given by

$$(\vec{F_e})_{ij} = -\kappa_e \left(d_{i,j} - L_{i,j} \right) T_{i,j} \vec{r}, \tag{7}$$

where $\vec{r} = \frac{(\vec{x_i} - \vec{x_j})}{|\vec{x_i} - \vec{x_j}|}$ is the directional unit vector between the position of element i and j, and κ_e is the spring constant, and $T_{i,j}$ is the minimum of the thickness of elements i, j. We choose $(\vec{F_b})_{ij}$ proportional to $T_{i,j}$ (the minimum thickness of elements i and j) so the formulation of interactive forces has the desired property that it obeys Newton's 3rd Law (i.e.: $(\vec{F_{IA}})_{ij} = -(\vec{F_{IA}})_{ji}$). This is in contrast to some other DEM models in the literature (e.g. Li et al [2014]). The minimum thickness is preferred to the average thickness, since this means that the for two bonded elements a fixed distance apart, acceleration due to elastic forces is bounded, even when the thickness of one of the elements approaches zero.

The frictional damping force has components that damp both the relative radial velocity and relative transverse velocities of the two elements. If $\vec{r}^{\perp}$ is the direction vector perpendicular to $\vec{r}$, and $P_{\vec{r}}$ and $P_{\vec{r}^{\perp}}$ are the projection matrices that project onto $\vec{r}$ and $\vec{r}^{\perp}$ respectively, then the frictional damping force is given by

$$(\vec{F_d})_{ij} = \left(-c_r P_{\vec{r}} - c_t P_{\vec{r}^{\perp}} \right) \cdot (\vec{u_i} - \vec{u_j}) \tag{8}$$

Here c_r and c_t are the radial and transverse drag coefficients. For the simulation below, we set $c_r = 2\sqrt{\kappa_e}$ and $c_t = \frac{1}{4}c_r$ so that the radial elastic force is critically damped, and the

transverse damping is sub critical. The damping forces are implemented using an implicit time stepping scheme, to avoid stability issues for very small elements (details found in Appendix B).

The effectiveness of the repulsive forces can be seen in Figure 3 which shows an un-coupled simulation where ice elements drift westward into a bay, and eventually come to rest with minimal overlap between elements. The effectiveness of the numerical bonds is demonstrated in Figure 4 tabular icebergs (constructed from many ice elements bonded together) and individual icebergs (unbonded elements) drift together towards a convex coast line. When the tabular icebergs arrive at the coast, they bump into the coastline and begin to rotate, influencing the paths of the other icebergs. In this example we see that modeling large structures using small elements bonded together, allows us to achieve large-scale structure and rotational motion, without having to include an equation for the angular momentum of the elements (as discussed in Jakobsen [2001]).

2.3. Element geometry and packing

Elements are packed differently depending on the shape of the elements. For all simulations in this study, we use elements whose surface areas are equally-sized regular hexagons. In order to pack these elements together, the hexagonal elements are initially arranged in a staggered lattice, with each element bonded to the adjacent elements (see Figure 5a). In this arrangement, each element (away from the edges) is bonded to six other elements. The bonds between elements form a pattern of equilateral triangles, which give the larger structure rigidity.

Some experiments were also performed using rectangular elements, arranged in a regular (non-staggered) lattice. In this case, each element forms four bonds with adjacent

₂₁₇ elements. However, the resultant structures were found to be much less rigid and tended

₂₁₈ to collapse when sufficient forces was applied. For this reason, hexagonal elements were

₂₁₉ preferred.

2.4. Ocean-ice and ice-ocean coupling

₂₂₀ The LIISM model is coupled to the ocean model via a two-way synchronous coupling,

₂₂₁ meaning that ocean model fields are passed to the LIISM model and the LIISM model

₂₂₂ fields are passed back to the ocean model at every time step. Passing fields between the

₂₂₃ two models involves interpolating fields between the Eulerian grid of the ocean model and

₂₂₄ the 'Lagrangian grid' of the LIISM model (i.e.: onto the ice elements).

₂₂₅ The coupling from the ocean model to the LIISM model is straight forward: at every

₂₂₆ time step, the ocean mixed layer temperature, salinity, velocity and sea-ice concentration

₂₂₇ are passed from the ocean model to the LIISM model, to be used in the momentum and

₂₂₈ thermodynamics equations of the ice elements. Within the LIISM model, the ocean model

₂₂₉ fields are interpolated onto the Lagrangian grid using a bilinear interpolation scheme. The

₂₃₀ LIISM model is not sensitive to the chosen interpolation scheme.

₂₃₁ The coupling in the other direction, from the LIISM model to the ocean model, is

₂₃₂ more complex. The LIISM model influences the ocean by: (i) applying a pressure to

₂₃₃ the ocean surface, (ii) applying a heat, salinity and mass flux to the ocean, associated

₂₃₄ with ice melting, and (iii) affecting the upper ocean boundary condition by applying a no

₂₃₅ slip boundary condition and frictional velocity beneath the ice. Fields from the LIISM

₂₃₆ model are interpolated from the Lagrangian grid to the Eulerian ocean grid before they

₂₃₇ are passed to the ocean model. Since the LIISM model applies large pressures to the

₂₃₈ ocean surface, the ocean model is sensitive to the interpolation scheme used to map the

239 LIISM fields to the ocean grid. Sudden jumps to the ocean surface pressure can trigger

240 tsunamis within the ocean model, making the ocean model become unstable.

241 The interpolation of the LIISM fields onto the ocean grid is done in a way that is

242 consistent with the shape of the elements in the LIISM model (see Section 2.3). Fields

243 are 'spread' to the ocean model by exactly calculating what fraction of an element's

244 surface area lies in a particular grid box, and dividing the field in proportion to this

245 fraction. For example, consider an element which has a hexagonal surface area in the

246 LIISM model, which is positioned such that it intersects four ocean grid cells (Figure

247 5b). In this situation, the mass of the element is divided between these four ocean cells

248 in proportion to the overlap area between the hexagonal element and the grid cell (this

249 fraction is shown by the colors in 5b). An advantage of this approach is that there are no

250 jumps in pressure as an element moves from one grid cell to another.

251 The numerical calculation of the intersection between hexagons and the ocean grid is

252 simplified by dividing the hexagon into 6 equilateral triangles. This method allows for the

253 intersection to be found even when the hexagon is not aligned with the grid. The LIISM

254 model can be run using hexagonal or rectangular elements.

255 The field-spreading scheme is coded with the restriction that an element's area can only

256 intersect a maximum of four ocean grid cells at a time. A consequence of this is that this

257 sets a limit on the maximum size of elements that can be represented using this model,

258 i.e.: the longest horizontal dimension of an ice element must be smaller than the ocean

259 grid spacing. Larger ice structures are constructed by bonding together smaller elements.

2.5. Thermodynamics

The ice elements decay according to a number of melt parameterizations. As the ice elements melt, their mass decreases, and the appropriate salt, mass and heat fluxes are passed to the ocean. In this section we described the melt parametrization for bonded, unbonded and partially bonded elements.

As mentioned above, ice elements which do not interact with other elements are modeled identically to the point particle icebergs described in Martin and Adcroft [2010]. These elements melt according to three semi-empirical parametrization for melt commonly used in previous iceberg studies [Gladstone et al , 2001; Martin and Adcroft , 2010]. Three types of iceberg melting are used: basal melt, M_b, melt due to wave erosion, M_e and melt due to buoyant convection, M_v. M_e and M_v are applied to the sides of the ice element, while M_b is applied at the ice element base. The details of M_b. M_v and M_e are given in Appendix A.

When multiple elements are bonded together to form larger structures, it is no long appropriate to use the parameterizations for melt developed for individual point-particle icebergs. An element which is completely surrounded by other elements, is meant to represent a piece of ice in the middle of a large structure, and hence will not experience a melt at its sides due to wave erosion or buoyant convection. Also, the iceberg basal melt rate, M_b described above is based on boundary layer theory of flow past a finite plate, and is only appropriate for basal surfaces where the distance from the leading edge is sufficiently small [Eckert , 1950; Weeks and Campbell , 1973]. For an element in the interior of large structures, the distance from the edge of the structure is large, and so using M_b for the basal melt is not appropriate. Instead, the basal melt, M_s is determined

using the three equation model for basal melt, which is a typical melting parametrization

beneath used beneath ice shelves [Holland and Jenkins , 1999].

When using both individual elements and bonded elements in the same simulation, we

determine which melt rate parameterizations to use based on the amount of bonds that

each element has. An element which is in the center of a large structure will form the

maximum number of bonds, while unbonded elements form zero bonds. If maximum

number of bonds that an element can form (given the shape of the element) is N_{max}, and

the number bonds that an element has is N_b, then the side melt and bottom melt for that

element are given by

$$M_{side} = \frac{(N_{max} - N_b)}{N_{max}}(M_v + M_e) \tag{9}$$

and

$$M_{bottom} = \frac{(N_{max} - N_b)}{N_{max}}M_b + \frac{N_b}{N_{max}}M_s \tag{10}$$

respectively. In this way, elements with no bonds, melt like point particle icebergs, ele-

ments at the center of large structures melt like ice shelves, and elements at the sides of

large structures have a combination of iceberg side and basal melt, and ice shelf melt.

2.6. Algorithms and computational efficiency

Including interactions between elements leads to an increase in the computational com-

plexity of the model. In this subsection we comment on some of the algorithmic proce-

dures that have been used to increase the computational efficiency. Readers who are not

interested in this more technical side of the model should skip this section.

2.6.1. Time stepping

₂₉₂ The ice elements in the LIISM model are advected using a semi-implicit velocity Verlet

₂₉₃ time-stepping scheme. The velocity verlet time stepping scheme is commonly used in DEM

₂₉₄ models in video games because it is computational efficient and has desirable stability

₂₉₅ properties [Jakobsen , 2001]. This time stepping scheme was preferred to the Runge-

₂₉₆ Kutta 4, which was used in the iceberg model of Martin and Adcroft [2010] since, the

₂₉₇ Verlet time stepping only requires one calculation of the interactive forces per time step

₂₉₈ (while the Runge-Kutta scheme requires the interactive forces to be calculated four times).

₂₉₉ Since the calculation of the interactive forces is one of the most computationally expensive

₃₀₀ part of the algorithm, the Verlet scheme leads to a significant increase in the speed of the

₃₀₁ model. We note that the Verlet scheme used in the LIISM contains a small modification

₃₀₂ of the original (fully explicit) velocity Verlet time stepping scheme in that damping terms

₃₀₃ are treated implicitly (which increases the numerical stability). The details of this time

₃₀₄ stepping schemed are outline in Appendix B.

2.6.2. Interactions and Bonds

₃₀₆ At every time step, we calculate the force on each element due to interactions with every

₃₀₇ other element. In principle, this involves order n^2 operations (for n elements). However,

₃₀₈ since each element only has repulsive interactions with elements that are less than one

₃₀₉ ocean grid cell away, and each element only has bonded interactions with a small number

₃₁₀ of other elements, we are able to reduce the complexity of the system.

₃₁₁ The complexity reduction is achieved by storing the element data in an efficient way

₃₁₂ that prevents having to search through all element pairs to check if they are close to

₃₁₃ one another or are bonded with one another. The data storage system works as follows:

₃₁₄ pointers to the memory structures containing each element are are stored in linked list data

315 structures, which allow elements to be added and removed from the lists easily without

316 restructuring the entire list. Instead of using one list for all the elements on a processor,

317 we use a separate linked list for each ocean grid cell. When an element moves between

318 ocean grid cells, it is removed from its original list and added to the list corresponding to

319 its new ocean grid cell. Since the area of elements has to be smaller than the area of an

320 ocean grid cell, the critical interaction critical interaction length scale (equation 5) is less

321 than the length of a grid cell. This means that elements only experience repulsive forces

322 with elements in the same ocean grid cell, or in one of the 8 adjacent cells. Limiting the

323 possible repulsive interactions to elements in the 9 linked lists substantially reduces the

324 computational time needed to calculate the total interactive force.

325   Bonded interactions are handled slightly differently. Each bond is assigned a piece of

326 memory. Each ice element contains a linked list of each of its bonds (typically up to six

327 bonds per element). At each time step, the code traverses the lists of bonded elements,

328 and adds a bonded force corresponding to these bond. The bonded force is only applied

329 if $\vec{r}_{i,j} > L_{ij}$, to avoid double counting an interaction. Having a list of bonds stored with

330 each element reduces the computational complexity of bonded interactions from order n^2

331 to order n. Handling bonded attractive forces separately to the repulsive and non-bonded

332 forces means that we do not need to check whether two elements are bonded, which further

333 increases the computational efficiency.

334 2.6.3. Parallelization and halos

335   The LIISM model runs on multiple processors in parallel. When elements move from

336 an ocean cell on one processor to an ocean cell on a second processor, the memory has to

337 be passed from one processor the next, added and removed to the appropriate lists and

338 the memory has to be allocated and deallocated correctly. Element interactions across

339 the edge of processors are handled using computational halos. A computational halo is a

340 copy of the edge of a one processor which is appended to the edge of a second processor,

341 so that the first processor can 'see' the second processor during a time step. Before a

342 time step, elements at the edges of each processor are copied onto the halos of adjacent

343 processors so that they can be used in calculating the interactive forces. After each time

344 step, these halos and removed, and the process is repeated. These halo updates are one

345 of the most computationally expensive parts of the LIISM model.

346 Keeping track of pairs of bonded elements that move across a processor edge requires

347 a lot of book keeping since bonds have to be severed and reconnected. Details of how

348 the bonds are broken and reconnected across processor boundaries are provided in Ap-

349 pendix C.

3. Experiment Setup

350 The introduction of Lagrangian elements, numerical bonds and interpolation schemes

351 between the Eularian and Lagrangian grids (discussed in Section 2) means that we are

352 now able to model ice shelf cavities which undergo large calving events. We demonstrate

353 this capability by performing numerical experiments with the LIISM model coupled to

354 the MOM6 ocean model [reference].

3.1. MISOMIP configuration

355 In order for our simulations to be easily comparable to previous models of ice shelf

356 cavities, we use an experimental setup based on the configuration created for the Marine

357 Ice Ocean Modeling Inter-comparion Project (MISOMIP) [Asay-Davis et al , 2016]. The

358 MISOMIP configuration was developed as a standardize configuration to allow for the

359 comparison between various ocean-ice coupled models. The configuration consists of an

360 idealized ice shelf in a rectangular domain. The domain is $L_x = 80$km wide and $L_y =$

361 480km long, and contains an ice shelf which is grounded on the south side of the domain

362 and has an ice front at y=650km. The ice thickness and bottom topography of this setup

363 are shown in Figure 6a and 6b respectively, with the grounding line position drawn in for

364 reference. The configuration is the same as that of the Ocean0 setup in the MISOMIP,

365 with three changes made:

366   1. The 'calving criteria' used in the MISOMIP study (which states that all points in

367 the ice shelf with thickness less than 100m are set to zero thickness) has not been used.

368   2. The ice shelf has been thickened on the flanks of the domain, so that the latitude of

369 the grounding line increases away from the center of the ice shelf.

370   3. The ice shelf is configured to be symmetric about its center line. This was achieved

371 by using the average of the left and right flank of the ice shelf thickness.

372   These three changes were made in order to make the circulation beneath the ice shelf

373 easier to interpret.

374   The LIISM model is coupled to the MOM6 ocean model. The ocean model is run in

375 layered mode, with a horizontal resolution of $\Delta x = 2$ km, and 36 vertical layers. Ocean

376 parameters are as specified in the MISOMIP configuration [Asay-Davis et al , 2016], and

377 are shown in Table 1. The simulation is initially at rest, with horizontally uniform initial

378 ocean temperature and salinity profiles that vary linearly between specified surface and

379 bottom values. The initial surface temperature and salinity are $T_t = -1.9°$C and $S_t = 33.8$

380 psu, respectively. The initial temperature and salinity at the depth H_{ocean} are $T_b = 1.0°$C

381 and $S_b = 34.7$ psu. The maximum ocean depth is $H_{ocean} = 720$ m. A sponge layer is used

382 on the northern boundary of which relaxes back to the initial temperature and salinity

383 with a relaxation time scale of $\tau = 0.1$ days. Melting is set to zero for cells where the

384 ocean column thickness is less than 10m to avoid using more energy to melt ice than is

385 present in the water column.

3.2. Initializing Lagrangian elements:

386 Ice elements in the LIISM model are set to be hexagonal and are arranged in a regular

387 staggered lattice (as discussed in Section 2.3). The apothem of the hexagons is initially set

388 to $A = 0.85$ km. Recall that the element size must be smaller than the ocean grid spacing

389 (i.e.: $2A < \Delta x$). The initial mass of the ice elements is determined by preprocessing

390 inversion, which is the inverse of the 'mass-spreading' interpolation procedure discussed

391 in Section 2.3. Boundary points are filled in using extra ice elements of appropriate

392 thickness.

393 When the model is run, the average ice draft in an ocean grid cell, is calculated from

394 the total mass of ice elements in that grid cell by assuming that the ice elements are in

395 hydrostatic balance. The total mass is found by summing up over all ice elements located

396 in that grid cell, while allowing elements to spread their mass across neighboring grid cells

397 (as discussed in Section 2.3). Figure 6b shows the draft of the ice shelf above the ice shelf

398 cavity in the coupled static ice shelf simulation using this interpolation method, while

399 Figure 6c shows the draft which is calculated without spreading an elements mass across

400 neighboring cells (i.e.: treating elements as point masses). When the mass spreading

401 interpolation scheme is not used, grid artifacts seen in the ice shelf draft (Figure 6c). The

402 grid artifacts are much reduced when the mass spreading interpolation is used (Figure

6b). In simulations without mass spreading, irregularities in ice draft cause irregularities in the ocean surface pressure, which cause spurious motion in the ocean (not shown). This is much reduced or absent when mass spreading is used.

3.3. Static ice shelf experiment

In the first experiment, we use a static ice shelf where the velocity of all ice elements is set to zero. In this experiment, the ice shelf is thermodynamically active and is able to 'melt' but has a constant thickness (as was done in the Ocean0 setup in the MISOMIP [Asay-Davis et al , 2016]). In this setup, ice shelf melting generates a temperature and salinity flux into the ocean, but does not change the thickness of the ice shelf. This can be thought to represent an ice shelf in dynamic equilibrium where the melt is exactly balanced ice shelf advection.

Results of the static ice shelf experiment using the LISSM model are compared to the results from an existing Eulerian ice shelf model [Goldberg et al , 2012], coupled to the same ocean model. The simulations in the Lagrangian and Eularian are compared after 5 years of models time.

3.4. Tabular iceberg calving

In the next set of experiments, we demonstrates capabilities of the LIISM model that can not be performed by traditional Eularian ice shelf models. These simulations model a large tabular iceberg being calved from the edge of the ice shelf. The tabular iceberg drifts in the ocean, submerged in the water column, where it influences the ocean circulation.

The tabular iceberg simulations are initialized using the final ocean state of the static ice shelf experiment. For these situations, all ice elements initially within a 15km radius of

423   the center of the ice front are allowed to move freely while the other ice elements continue

424   to be held are stationary. The three tabular iceberg simulations are performed:

425   1. **Tabular iceberg with fixed velocity**:

426   In this simulation, the velocity of the non-stationary elements is fixed to u=0m/s,

427   v=0.01m/s. This simulation allows us to study the response of the ocean to distur-

428   bance caused by a tabular iceberg moving through the water (with an fixed velocity).

429   This simulation is not fully coupled since the velocity of the elements is prescribed.

430   2. **Tabular iceberg with bonded elements**:

431   All non-stationary ice elements are bonded together by the numerical bonds. This ex-

432   periments is fully-coupled in that the ice elements are driven the ocean, and the pressure

433   exerted by the ice elements drives ocean flow. In order to make the iceberg drift away

434   from the ice shelf, we imposed a zonal wind stress of $\tau_x = 0.1 \frac{N}{m^2}$. .

435   3. **Tabular iceberg with unbonded elements**:

436   This simulation is identical to the bonded elements simulation, except that all the numer-

437   ical bonds are broken, so that the elements are free to move away from one another.

4. Results

4.1. Static ice shelf experiment

438   **Comparison of LIISM and Eularian ice shelf model**

439   The results from coupled ocean-ice simulation in the MISOMIP configuration using LIISM

440   are compared to the results using an Eulerian ice shelf model in the same configuration.

441   The ice draft in the Eulerian ice shelf model is initialized using the field shown in Figure

442   6b. Figures S2 show the time-averaged melt rates of both the Lagrangian and Eulerian

443   ice shelf models, averaged over the first 5 years of the simulation.

⁴⁴⁴ The melt rates of the Eulerian and Lagrangian models are very similar with slight

⁴⁴⁵ difference showing up at the grounding line and ice front (Figure S2). The slight difference

⁴⁴⁶ at the grounding line are a result of the fact that elements in the LIISM model are smaller

⁴⁴⁷ than a grid cell in length. This means that ice element near the grounding line may be

⁴⁴⁸ ungrounded in the LIISM model, while the grid cell is considered grounded in the Eularian

⁴⁴⁹ model. At the ice front, the Eularian model has a straight ice front, while the LIISM model

⁴⁵⁰ has a staggered ice front, which is a result of the staggered hexagonal packing.

⁴⁵¹ The small changes in melt at the grounding line and ice front drive slight changes to the

⁴⁵² circulation beneath the ice shelf, which in turn lead to small difference in the temperature

⁴⁵³ and salinity profiles over time. This is seen by comparing the time-averaged ocean salinity

⁴⁵⁴ profiles for the Lagrangian and Eularian ice shelves (Figure S1) and also by comparing the

⁴⁵⁵ the time-averaged barotropic stream function of the two simulations (see Figures 8) and

⁴⁵⁶ in the supplementary material). The differences between the Eularian and Lagrangian

⁴⁵⁷ simulations are small compared to the wide spread of difference seen in the MISOMIP

⁴⁵⁸ inter comparison. This is unsurprising, since the LIISM and Eularian ice shelves are

⁴⁵⁹ coupled to the same ocean model and pass similar fields to the ocean model.

⁴⁶⁰ The similarity of the Lagrangian and Eulerian ice shelf models shows that the LIISM

⁴⁶¹ model coupled to an ocean model is able to model sub ice shelf cavities as well as the

⁴⁶² Eularian model does. This is a good starting point for moving beyond the capabilities of

⁴⁶³ the Eularian model.

4.2. Tabular iceberg calving

⁴⁶⁴ **Tabular iceberg with fixed velocity**

⁴⁶⁵ The fixed iceberg velocity calving experiment demonstrates that the model is able to

466 simulate a tabular iceberg being calved from an ice shelf. After the iceberg calves, it

467 moves northwards away from the ice shelf with a prescribed velocity. After the iceberg

468 has calved away from the ice shelf, we observed a warming of the surface waters near the

469 near the ice front and iceberg edge. This surface warming is caused by an upwelling of the

470 warmer waters from beneath the ice shelf and iceberg. As the icebergs drifts away from

471 the ice front, these warmer waters remain in the wake of the iceberg (Figures 2). The

472 signature of upwelling water in the wake of a drifting tabular iceberg bears some similarity

473 to satellite observations of streaks of increased ocean color near to tabular iceberg in the

474 Southern Ocean [reference], suggesting that the increased productivity around iceberg

475 may be driven by upwelling water delivering nutrients to the surface. The motion of the

476 iceberg also drives barotropic velocities through out the water column, which disturb the

477 initial stratification of the water column (Figures 1).

478 **Fully coupled tabular iceberg**

479 The necessity of bonds between ice elements is demonstrated by comparing two simulations

480 where an iceberg calves, and is allowed to evolve freely with the flow. In the Bonded

481 simulation, the elements in the calved iceberg are bonded together, while in the Unbonded

482 simulation the all bonds between elements in the tabular iceberg are broken.

483 In the Bonded simulation, the ice element in the tabular iceberg remain close to one

484 another, and the tabular iceberg retains its shape (Figure 9a,c). The elements are forced

485 by the melt-water-driven current at the ice front, which moves towards the north-west

486 (see Figure S3 in the supplementary material). This current, together with the Coriolis

487 force, cause the iceberg to rotate before moving away from the ice shelf (Figure 9a).

In the Unbonded simulation, the ice elements in tabular iceberg are not constrained

to move together. Instead, the elements spread out and drift towards the north-west for

the same reason discussed above. Since the ice elements are not closely, packed together,

they apply a smaller pressure to the ocean surface, spread over a larger area (Figure 9c).

The type of behavior could be relevant in simulating ice shelf disintegrations, rather than

tabular iceberg calving.

5. Discussion

1) How do we get this into a big coupled climate model - what is still needed? Bond

breaking, ice growing 2) Mention lagrangian sea ice

6. Appendix A

6.1. Environmental forces on ice elements

The non-interactive forces on an ice element are as described in [Martin and Adcroft ,

2010], and are repeated here for completeness. The force on an element due to air (a),

ocean (o) and sea ice (si) drag are given by

$$(\vec{F_a}) = \rho_a(0.5c_{a,v}WF + c_{a,h}LW)|\vec{u}_a - \vec{u}|(\vec{u}_a - \vec{u}), \tag{11}$$

$$(\vec{F_o}) = \rho_o(0.5c_{o,v}W(D - T_{si})F + c_{o,h}LW)|\vec{u}_o - \vec{u}|(\vec{u}_o - \vec{u}), \tag{12}$$

$$(\vec{F_{si}}) = \rho_{si}(0.5c_{si,v}WT_{si}F + c_{si,h}LW)|\vec{u}_{si} - \vec{u}|(\vec{u}_{si} - \vec{u}). \tag{13}$$

Here ρ_a, ρ_o, ρ_{si}, are the density of air, ocean and sea ice, respectively. $c_{a,v}$, $c_{o,v}$ and $c_{si,v}$

are the vertical drag coefficients with air, ocean and sea ice, while $c_{a,h}$, $c_{o,h}$ and $c_{si,h}$ are

the respective horizontal drag coefficients. Here $\vec{u}_a$, $\vec{u}_o$, $\vec{u}_{si}$, are the velocities air, ocean

and sea ice, respectively. L, W, T, F and D are the length, width, thickness, freeboard

and draft of the ice element. The element thickness is related to the draft and freeboard by $T = F + D$ and $D = \frac{\rho}{\rho_o}T$, where ρ is the ice element density.

The wave radiation force $(\vec{F}_R)$ is given by

$$\vec{F}_R = \frac{1}{2}\rho_o c_r g a \,\min(a, F)\, 2\frac{WL}{W + L}\frac{\vec{v}_a}{|\vec{v}_a|} \tag{14}$$

where g is the acceleration due to gravity, a is the wave amplitude empirically related to the wind speed by $a = 0.010125|\vec{v}_a - \vec{v}_o|$, and c_{wd} is the wave drag coefficient defined as

$$c_{wd} = 0.06 \min\left(\max\left[0, \frac{L - L_c}{L_t - L_c}\right], 1 \right), \tag{15}$$

where $L_w = 0.32|\vec{v}_a - \vec{v}_o|^2$ is an empirical wave length, $L_c = 0.125 L_w$ is the cutoff length, and $L_t = 0.25 L_w$ is the upper limit.

The pressure gradient force is approximated as a force due to sea surface slope and given by

$$\vec{F}_{SS} = -Mg\vec{\nabla}\eta \tag{16}$$

where η is the sea surface height.

6.2. Melt rate parametrization

As discussed in Section 2.5, unbounded ice elements in the LIISM model decay according to parameterizations for iceberg decay typically used in iceberg drift models [Martin and Adcroft , 2010], while ice elements within larger ice structures have only a basal melt given by the three equation model [Holland and Jenkins , 1999] .

For unbonded ice elements, the element thickness decays at due to basal melt at a rate M_b, while the length and width of the elements decay as a result of melt due to wave erosion, M_e and melt due to buoyant convection, M_v. Following Martin and Adcroft [2010], the basal melt rate, wave erosion melt rate, and buoyant convection melt rate are

parameterized by

$$M_b = 0.58 |\vec{v} - \vec{v_0}|^{0.8} \frac{\tilde{T_0} - \tilde{T}}{L^{0.2}} \tag{17}$$

$$M_e = \frac{1}{12} S_s \left(1 + \cos\left[\pi A_i^3\right]\right) \left(\tilde{T_0} + 2\right), \tag{18}$$

$$M_v = \left(7.62 \times 10^{-3}\right) \tilde{T_0} + \left(1.29 \times 10^{-3}\right) \tilde{T_0}^2. \tag{19}$$

$\tilde{T}$ is the effective iceberg temperature and is set to $\tilde{T} = 4°\text{C}$, $\tilde{T_0}$ is the temperature at the top of the ocean, A_i is the sea ice area fraction, and S_s is the sea state, which is given by the Beaufort scale

$$S_s = \frac{2}{3} |\vec{u_a} - \vec{u_o}|^{\frac{1}{2}} + \frac{1}{10} |\vec{u_a} - \vec{u_o}| \tag{20}$$

509 All three melt rates are in units of meters per day.

510 For elements inside larger structures, the melt due to wave erosion and melt due to

511 buoyant convection are set to zero, and the basal melt, M_s is given by the standard three

512 equation model [Holland and Jenkins , 1999].

7. Appendix B

7.1. Modified Verlet Algorithm

513 The LIISM model uses a version velocity verlet algorithm, which has been modified

514 to allow part of the forcing to be calculated implicitly. The traditional velocity verlet

515 algorithm is commonly used in molecular dynamics, as it is simple to implement, second

516 order accurate and computationally efficient [Swope et al , 1982; Omelyan et al , 2002].

517 Here we modify the tradition scheme to allow for the drag forces to be modeled implicitly,

518 which prevents large accelerations for element's whose mass approaches zero. To do

519 this, we modify the traditional verlet algorithm to include both an implicit and explicit

520 acceleration, $a(t) = a_{exp}(t) + a_{imp}(t)$. The explicit acceleration, $a_{exp}(t)$ includes all forcing

521 terms which depend only on the previous time step, while the implicit acceleration, $a_{imp}(t)$

522 includes forcing terms which depend on the current time step (in particular the drag and

523 Coriolis forces).

524 Using a time step of Δt and the notation $t_{n+1} = t_n + (\Delta t)$, the modified velocity verlet

525 scheme can be written as:

526 1) $x(t_{n+1}) = x(t_n) + u(t_n)\Delta t + \frac{1}{2}\Delta t^2 \left(a_{exp}(t_n) + a_{imp}(t_n) \right).$

527 2) Calculate $a_{exp}(t_{n+1})$ and $a_{imp}(t_{n+1})$

528 3) $u(t_{n+1}) = u(t_n) + \frac{\Delta t}{2} \left(a_{exp}(t_n) + a_{exp}(t_{n+1}) \right) + (\Delta t)a_{imp}(t_{n+1})$

529 This scheme reduces to the traditional velocity verlet when a_{imp} is set to zero. Note that

530 at step 2, $a_{exp}(t_{n+1})$ is an explicit function of $x(t_{n+1})$ and other qualities evaluated at time

531 t_n, while $a_{imp}(t_{n+1})$ additionally depends on $u(t_{n+1})$ (and needs to be solved implicitly).

532 For this reason, steps 2 and 3 need to be solved simultaneously, as described in the next

533 section.

534 In equation (1), the forces due to ocean drag, atmospheric drag and sea ice drag are

535 treated implicitly. The force due to sea surface slope and wave radiation are treated

536 explicitly. The Coriolis term is handled using Crank-Nicolson scheme so that half of the

537 effect is implicit and half is explicit. The elastic part of the interactive forces is treated

538 explicitly, while the interactive damping is handled semi-implicitly in that the drag force

539 on element A by element B depends on the velocity of elements A and B evaluated at

540 time t_{n+1} and t_n, respectively.

7.2. Solving for the velocity implicitly

Since this modified scheme contains some forcing terms which are handled implicitly,

steps 2 and 3 need to be solved together. We demonstrate how this is done, using a

simplified one-dimensional version of equation (1), neglecting the atmospheric drag, sea ice drag and Coriolis force, so that the only implicitly treated term is the ocean drag. We also define an explicit force F_{exp}, which accounts for all forces not proportional the element velocity. With these simplifications, the implicit and explicit accelerations are

$$a_{exp} = \frac{1}{M}(\vec{F}_{exp}) \tag{21}$$

$$a_{imp} = \frac{1}{M}(F_W) \tag{22}$$

The ocean drag force at time t_{n+1} is modeled (mostly) implicitly as

$$F_W(t_{n+1}) = c_w|u_w(t_n) - u(t_n)|(u_w(t_n) - u(t_{n+1})) \tag{23}$$

Step 3 of the modified velocity verlet scheme can be rewritten by introducing an intermediate velocity u^*, which only depends on the velocity and acceleration at time t_n,

$$u^*(t_n) = u(t_n) + \frac{1}{2}(\Delta t)a(t_n). \tag{24}$$

Using this, the updated velocity (Step 3) can be written

$$u(t_{n+1}) = u^*(t_n) + \frac{\Delta t}{2}a_{exp}(t_{n+1}) + (\Delta t)a_{imp}(t_{n+1}). \tag{25}$$

Including the forcing terms into this equations gives

$$u(t_{n+1}) = u^*(t_n) + \frac{\Delta t}{2M}(F_{exp}(t_{n+1})) + \frac{\Delta t}{M}\left(c_w|u_w(t_n) - u(t_n)|(u_w(t_n) - u(t_{n+1}))\right) \tag{26}$$

Solving for $u(t_{n+1})$ in terms of quantities which only depend on the previous time step gives

$$u(t_{n+1}) = \frac{u^*(t_n) + \frac{\Delta t}{2M}(F_{exp}(t_{n+1})) + \frac{\Delta t}{M}\left(c_w|u_w(t_n) - u(t_n)|(u_w(t_n))\right)}{\left(1 + \frac{\Delta t}{M}c_w|u_w(t_n) - u(t_n)|\right)} \tag{27}$$

541 Once the $u(t_{n+1})$ has been found, it can be used to calculated the explicit and implicit

542 accelerations, which are required for the next time step.

543 Finally, we note that the the drag term (equation 23) is not entirely implicit, since the

544 element velocity inside the absolute value is evaluated at time t_n, rather than at time

545 t_{n+1}. This is done so that we can solve for the updated velocity exactly. One consequence

546 of this is that it gives rise to a small oscillation in the element velocity. This oscillation is

547 addressed by using a predictive corrective scheme: once you have solved for a first guess

548 of the velocity at time t_{n+1}, this estimate of the velocity is used to update the estimate

549 of the drag force (i.e.: inside the absolute value signs). Using the updated drag, you can

550 now repeat the process described above to find an improved estimate of the velocity. We

551 found that two iterations were sufficient to remove the unwanted oscillation.

552 The procedure described in this section is easily extended to include more forcing terms

553 and two dimensions (where it involves inverting a 2×2 matrix).

8. Appendix C

554 **Connecting bonds across processor boundaries**

555 When a bonded element moves off the edge of a processor, the bond needs to be bro-

556 ken. When the element is copied into the halo of the processor, the bond needs to be

557 reconnected.., and then reconnected when the element is copied back

558 The basics of the bond bookkeeping work as follows. Consider an element A and an

559 element B that are bonded together. As mentioned above, each element has a copy of

560 the bond which is stored with the element. Let A-B be the bond stored by element A,

561 and B-A be the bond stored by element B. Bond A-B contains a pointer which points to

562 element B and bond B-A contains a pointer which points to element A.

Consider a situation where element A and B are originally on Processor 1, and then element B moves to Processor 2. When this occurs, the memory assigned to element B on processor 1 is removed, and is allocated on Processor 2. This means that the pointer to element B in bond A-B (stored in element A on Processor 1) is no longer assigned. Similarly, the pointer to element A in bond B-A (stored in element B on Processor 2) is no longer assigned. Before the next time step, a halo update occurs, so that the there is a copy of element A in the halo of Processor 2 and a copy of element B in the halo of Processor 1. After the halo update, the bonds A-B and B-A have to be reconnected on both Processor 1 and 2. To aid in reconnecting the bonds, a copy of the grid cell number of element B is stored in the bond A-B and a copy of the grid cell number of element A is stored in the bond B-A. We refer to this as the 'most recent address'. Before a bond is moved from one processor to another, the 'most recent address' is updated, so that the bond can be reconnected later. To reconnect bond A-B on Processor 1 (for example), we find the most recent address of element B, and search through the list of elements in the grid cell corresponding to the most recent address of element B until element B is found. The pointer to element B in bond A-B is reassigned and the bond is said to be connected.

Once all bonds are reconnected, a bond quality control is done where we loop through all bonds and check that they are working properly. To check that a bond is working properly is a four step process. For example, consider the bond A-B stored in element A on Processor 1. To check the quality of this bond A-B, we use the following four steps:

1. Check that the pointer to element B is assigned on bond A-B (stored on element A).

2. Check that the corresponding bond B-A exists on element B.

586   3. Check that a pointer to element A exists in this bond B-A.

587   4. Check that the element A which is being pointed to is the same element A where

588 you started.

589   All four of these tests must pass in order to make sure that the memory is correctly

590 assigned. A useful tool in this process is that each element is assigned a unique number

591 so that elements are easily identified.

9. Possibly add

9.1. Lagrangian sea ice mode

The addition of interactive forces between elements, means that the LIISM model can be used as a Lagrangian sea ice model, following [Li et al, 2014]. In this formulation, each element represents a collection of sea ice flows.

9.2. Orientation

We can get the orientation of iceberg by considering the bonds that they form.

9.2.1. DEM vs SPH

Note that there is some ambiguity in the literature about the definition of a Discrete Element Model. In one view, to qualify as a Discrete Element Model since we do not evolve the angular momentum of the elements. Since elements are allows to overlap briefly, this method could be considered an example of a Smooth Particle Hydrodynamics model. This same repulsive force is similar to that used by [Li et al] in the context of sea ice interactions.

References

Asay-Davis, X. S., S. L. Cornford, B. K. Galton-Fenzi, R. M. Gladstone, G. H. Gudmunds-son, D. M. Holland, P. R. Holland, and D. F. Martin (2016), Experimental design for three interrelated marine ice sheet and ocean model intercomparison projects: MIS-MIP v. 3 (MISMIP+), ISOMIP v. 2 (ISOMIP+) and MISOMIP v. 1 (MISOMIP1). *Geoscientific Model Development* 9, no. 7: 2471.

Arrigo, K. R., G. L. van Dijken, D. G. Ainley, M. A. Fahnestock, and T. Markus (2002). Ecological impact of a large Antarctic iceberg. *Geophys. Res. Let.*, 29(7).

Alley, R. B., H. J. Horgan, I. Joughin, K. M. Cuffey, T. K. Dupont, B. R. Parizek, S. Anandakrishnan, and J. Bassis (2008), A simple law for ice-shelf calving. *Science* 322, no. 5906, 1344-1344.

Bassis, J. N., and S. Jacobs (2013), Diverse calving patterns linked to glacier geometry. *Nature Geoscience*, 6(10), 833-836.

Benn, D. I., C. R. Warren, and R. H. Mottram (2007). Calving processes and the dynamics of calving glaciers. *Earth-Science Reviews*, 82(3), 143-179.

Bigg, G. R., Wadley, M. R., Stevens, D. P., and Johnson, J. A. (1997), Modelling the dynamics and thermodynamics of icebergs. *Cold Regions Science and Technology*, 26(2), 113-135.

Biddle, L. C., J. Kaiser, K. J. Heywood, A. F. Thompson and A. Jenkins (2015), Ocean glider observations of iceberg-enhanced biological productivity in the northwestern Wed-dell Sea, *Geophys. Res. Lett.*, 42, 459465.

De Rydt, J., and G. H. Gudmundsson (2016), Coupled ice shelf?ocean modeling and complex grounding line retreat from a seabed ridge. *J. of Geophys. Res.: Earth Surface*,

121(5), 865-880.

Dunne, J.P., J.G. John,, A.J. Adcroft, S.M. Griffies, R.W. Hallberg, E. Shevliakova, R.J. Stouffer, W. Cooke, K.A. Dunne, M.J Harrison, and J.P. Krasting (2012), GFDL's ESM2 global coupled climate-carbon Earth System Models. Part I: Physical formulation and baseline simulation characteristics. *J. of Climate*, 25(19), 6646-6665.

Depoorter, M. A., J. L. Bamber, J. A. Griggs, J. T. M. Lenaerts, Stefan RM Ligtenberg, M. R. van den Broke, and G. Moholdt (2013), Calving fluxes and basal melt rates of Antarctic ice shelves. *Nature*, 502(7469), 89-92.

Determan J., Gerdes R. (1994), Melting and freezing beneath ice shelves: implications from a three-dimensional ocean-circulation model. *Ann. Glaciol.*, 20, 413-419.

Dowdeswell, J. A., and J. L. Bamber (2007). Keel depths of modern Antarctic icebergs and implications for sea-floor scouring in the geological record. *Marine Geology*, 243(1), 120-131.

Eckert, E. R. G. (1950). Introduction to the Transfer of Heat and Mass. McGraw-Hill.

Gladstone, R. M., G. R. Bigg, and K. W. Nicholls. (2001), Iceberg trajectory modeling and meltwater injection in the Southern Ocean (19782012). *J. of Geophys. Res.: Oceans*, 106(C9), 19903-19915.

Goldberg, D. N., C. M. Little, O. V. Sergienko, A. Gnanadesikan, R. Hallberg, and M. Oppenheimer (2012), Investigation of land ice?ocean interaction with a fully coupled ice?ocean model: 1. Model description and behavior. *J. of Geophys. Res.: Earth Surface*, 117(F2).

Gladish, C. V., D. M. Holland, P. R. Holland, and S. F. Price (2012), Ice-shelf basal channels in a coupled ice/ocean model. *J. of Glaciol.*, 58(212), 1227-1244.

Grosfeld K., R. Gerdes, J. Determan (1997), Thermohaline circulation and interaction between ice shelf cavities and the adjacent open ocean. J. Phys. Oceanogr., **102**, C7, 15959-15610.

Grosfeld, K., and H. Sandhger, (2004). The evolution of a coupled ice shelfocean system under different climate states. *Global and Planetary Change*, 42(1), 107-132.

Holland D. M., Jenkins A. (2001), Adaptation of an isopycnic coordinate ocean model for the study of circulation beneath ice shelves. *Mon. Wea. Rev.*, 129, 1905-1927.

Holland P. R. and D. L. Feltham (2006), The effects of rotation and ice shelf topography on frazil-laden Ice Shelf Water plumes. *J. Phys. Oceanogr.*, 36, 2312-2327.

Holland, D. M., and A. Jenkins (1999), Modeling thermodynamic ice-ocean interactions at the base of an ice shelf. J. of Phys. Oceanogr. 29.8, 1787-1800.

Hellmer H.H., Olbers D. J. (1989), A two-dimensional model for the thermohaline circulation under an ice shelf. *Antarctic Science*, 1, 325- 336.

Jakobsen, T. (2001). Advanced character physics. *In Game Developers Conference*, Vol. 3.

Jenkins, A., P. Dutrieux, S. S. Jacobs, S. D. McPhail, J. R. Perrett, A. T. Webb, and D. White (2010), Observations beneath Pine Island Glacier in West Antarctica and implications for its retreat. it Nature Geo., 3(7), 468-472.

Jacobs, S. S., A. Jenkins, C. F. Giulivi, and P. Dutrieux (2011). Stronger ocean circulation and increased melting under Pine Island Glacier ice shelf. Nature Geo., 4(8), 519-523.

Jongma, J. I., E. Driesschaert, T. Fichefet, H. Goosse, and H. Renssen (2009), The effect of dynamic-thermodynamic icebergs on the Southern Ocean climate in a three-dimensional model, *Ocean Modell.*, 26, 104113.

Lewis E.L. and R.G. Perkin (1986), Ice pumps and their rates. *J. of Geophys. Res.*, 91,
    11756-11762.

Losch, M. (2008). Modeling ice shelf cavities in az coordinate ocean general circulation
    model. *J. of Geophys. Res.: Oceans*, 113(C8).

Li, B., H. Li, Y. Liu, A. Wang and S. Ji (2014), A modified discrete element model for
    sea ice dynamics. *Acta Oceanologica Sinica*, 33(1), 56-63.

Lichey, C., and H. H. Hellmer (2001). Modeling giant-iceberg drift under the influence of
    sea ice in the Weddell Sea, Antarctica. *J. of Glaciol.*, 47(158), 452-460.

Levermann, A., T. Albrecht, R. Winkelmann, M. A. Martin, M. Haseloff, and I. Joughin.
    (2012), Kinematic first-order calving law implies potential for abrupt ice-shelf retreat.
    The Cryosphere, 6(2), 273-286.

Martin, T., and Adcroft, A. (2010), Parameterizing the fresh-water flux from land ice
    to ocean with interactive icebergs in a coupled climate model. *Ocean Modelling*, 34(3),
    111-124.

Marsh, R., V. O. Ivchenko, N. Skliris, S. Alderson, G. R. Bigg, G. Madec, A. T. Blaker
    Y. Aksenov, B. Sinha, A.C. Coward, and J.L. Sommer (2015), NEMOICB (v1. 0):
    interactive icebergs in the NEMO ocean model globally configured at eddy-permitting
    resolution. *Geoscientific Model Development* 8, no. 5 (2015): 1547-1562.

MacAyeal D.R. (1984), Thermohaline Circulation Below the Ross Ice Shelf: A Conse-
    quence of Tidally Induced Vertical Mixing and Basal Melting. *J. Geophys. Res.*, 89,
    597-606

Nicholls K.W. (1996), Temperature variability beneath Ronne Ice Shelf, Antarctica, from
    thermistor cables. *J. Phys. Oceanogr.*, 11, 1199-1210.

Nicholls KW, Østerhus S, Makinson K (2009), Ice-Ocean processes over the continental shelf of the southern Weddell Sea, Antarctica: a review. *Rev. Geophys.* 47(3).

Omelyan, I. P., M. I. Mryglod, and R. Folk (2002), Optimized Verlet-like algorithms for molecular dynamics simulations. *Physical Review E*, 65(5), 056706.

Rignot, E., S. Jacobs, J. Mouginot, and B. Scheuchl (2013), Ice-shelf melting around Antarctica. *Science*, 341, no. 6143 (2013): 266-270.

Robinson, N. J., M. J. M. Williams, P. J. Barrett, and A. R. Pyne (2010), Observations of flow and ice-ocean interaction beneath the McMurdo Ice Shelf, Antarctica, *J. Geophys. Res.*, 115, C03025

Sergienko, O. V. (2013). Basal channels on ice shelves. *J. of Geophys. Res.: Earth Surface*, 118(3), 1342-1355.

Silva, T. A. M., Bigg, G. R., and Nicholls, K. W. (2006), Contribution of giant icebergs to the Southern Ocean freshwater flux. J. of Geophys. Res.: Oceans, 111(C3).

Smith, K., B. Robison, J. Helly, R. Kaufmann, H. Ruhl, H., T. Shaw, and M. Vernet (2007), Free-drifting icebergs: Hotspots of chemical and biological enrichment in the Weddell Sea, *Science*, 317, 478482.

Stern, A. A., D. M. Holland, P. R. Holland, A. Jenkins and J. Sommeria (2014), The effect of geometry on ice shelf ocean cavity ventilation: a laboratory experiment. *Experiments in Fluids*, 55(5), 1-19.

Stern, A.A., Johnson, E., Holland, D.M., Wagner, T.J., Wadhams, P., Bates, R., Abrahamsen, E.P., Nicholls, K.W., Crawford, A., Gagnon, J. and Tremblay, J.E. (2015), Wind-driven upwelling around grounded tabular icebergs. *J. of Geophys. Res.: Oceans*, 120(8), 5820-5835.

[717] Stern, A. A., A. Adcroft, and O. Sergienko (2016), The effects of Antarctic iceberg calv-

[718] ing?size distribution in a global climate model. *J. of Geophys. Res.: Oceans*, 121(8),

[719] 5773-5788.

[720] Swope, W. C., H. C. Andersen, P. H. Berens, and K. R. Wilson (1982), A computer

[721] simulation method for the calculation of equilibrium constants for the formation of

[722] physical clusters of molecules: Application to small water clusters. *The Journal of*

[723] *Chemical Physics* 76, no. 1, 637-649.

[724] Tournadre, J., N. Bouhier, F. Girard-Ardhuin, and F. Rmy (2016), Antarctic icebergs

[725] distributions 1992-2014. *J. Geophys Res: Oceans*.

[726] Vernet, M., et al. (2012), Islands of ice: Influence of free-drifting Antarctic icebergs on

[727] pelagic marine ecosystems, Oceanography, 25(3), 3839

[728] Weeks, W. F., and W. J. Campbell (1973). Icebergs as a fresh-water source: an appraisal.

[729] *J. of Glaciol.*, 12(65), 207-233.
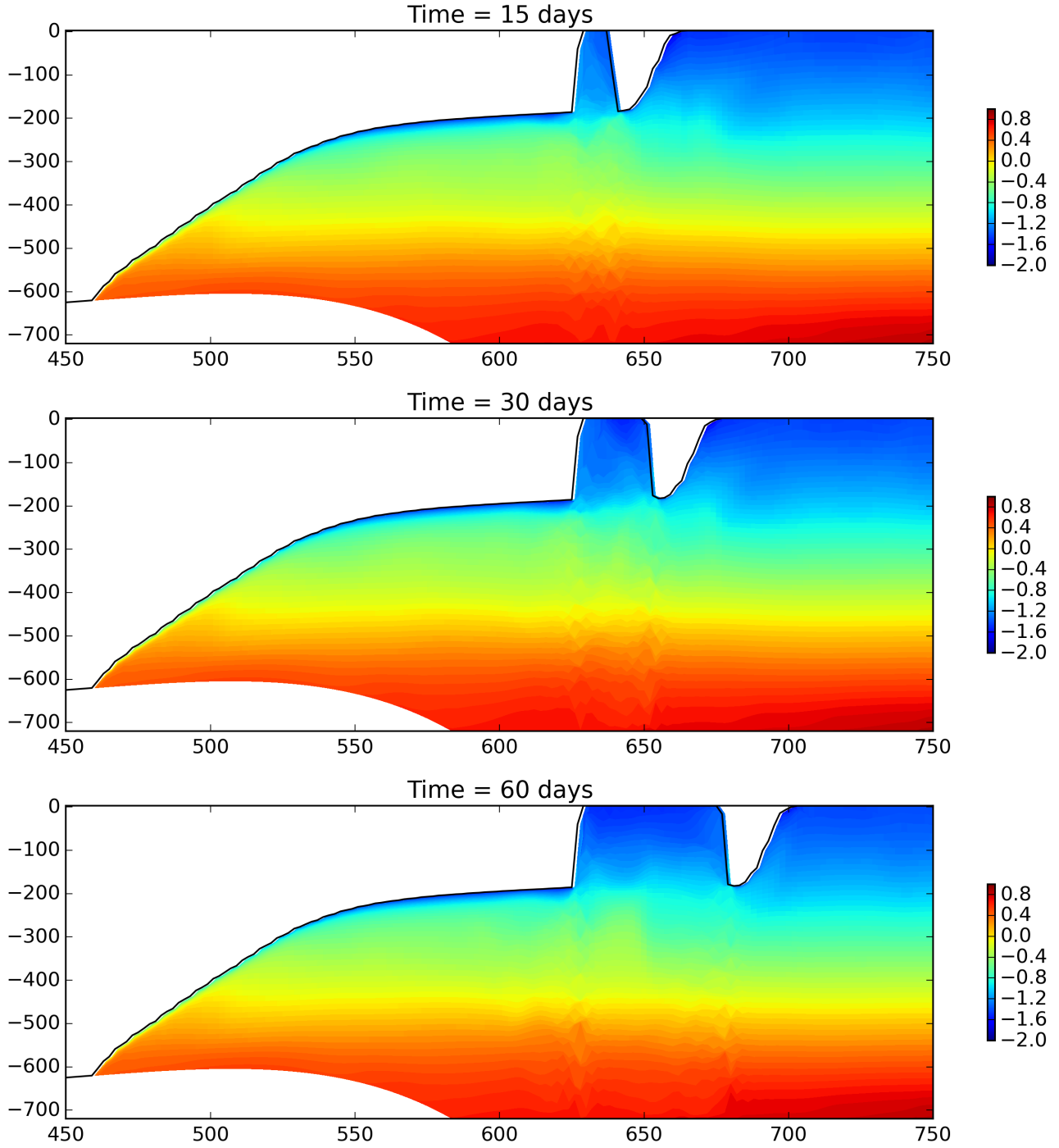
Figure 1. Temperature section at $y = \frac{L_y}{2}$ for the tabular iceberg calving with fixed velocity simulation (using the LIISM ice shelf) at time (a) t=15, (b) t=30, and (c) t=60 days.
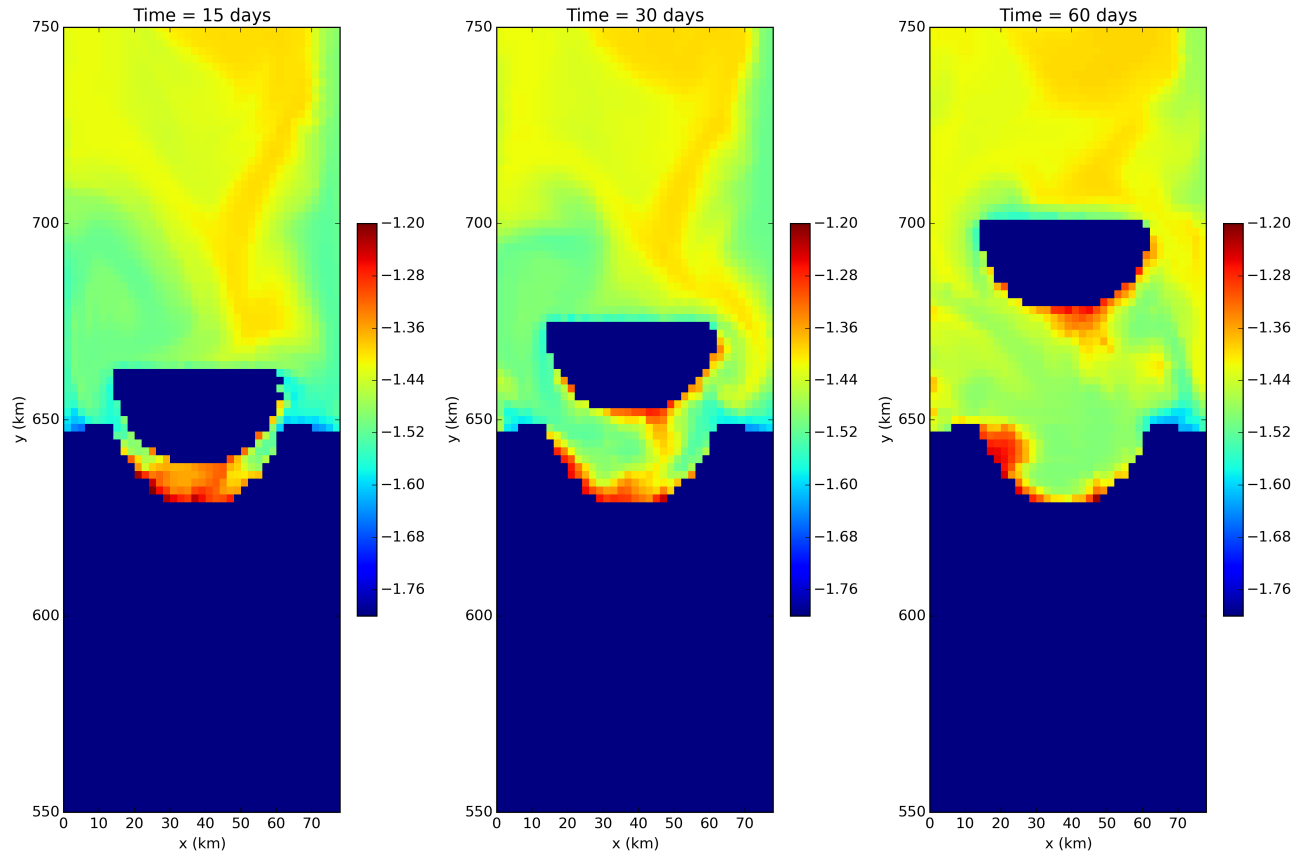
Figure 2. Sea surface temperature for the tabular iceberg calving with fixed velocity simulation at time (a) t=15, (b) t=30, and (c) t=60 days.
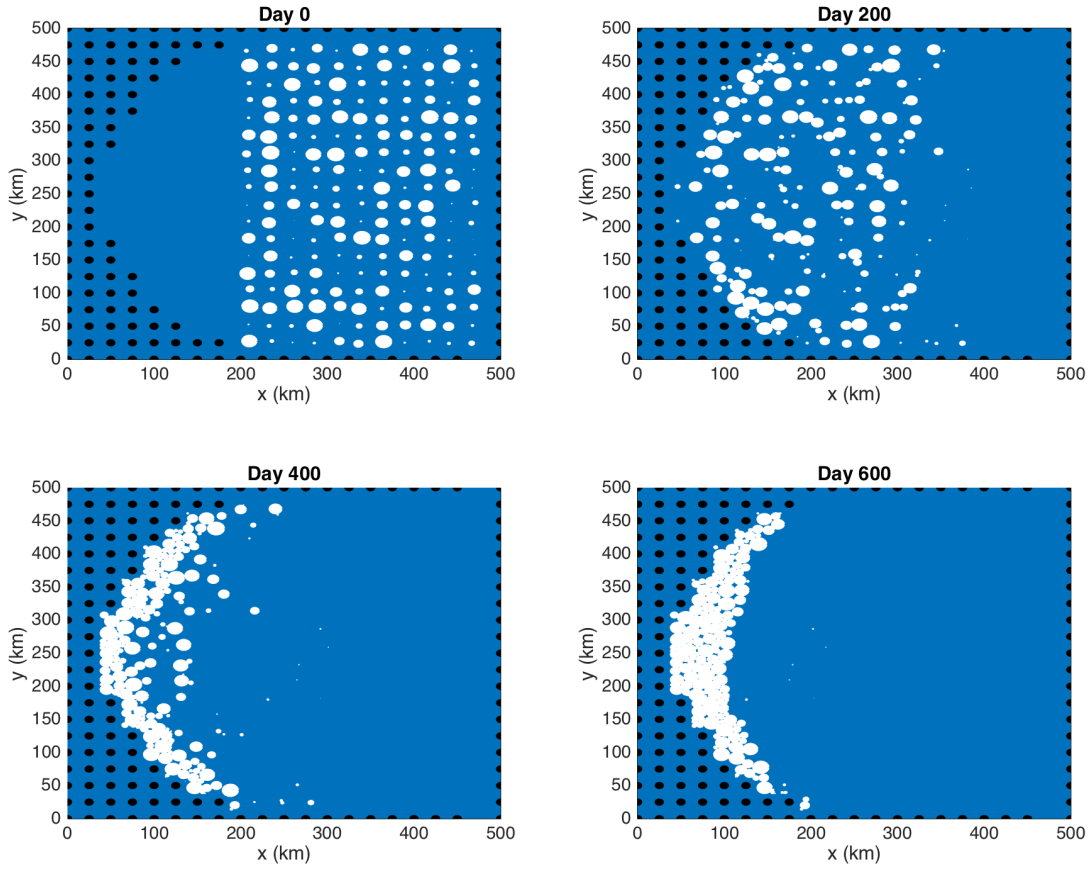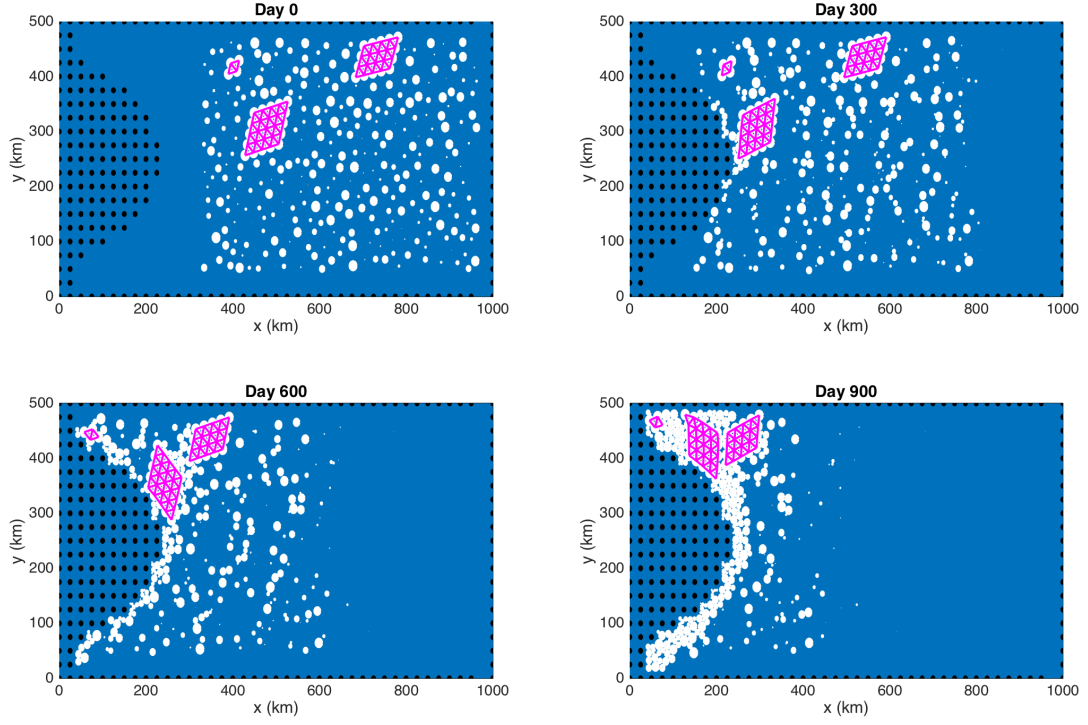
Figure 3.   Positions of ice elements at time t=0, 200, 400, 600 days for the simulation. The size of the dots shows the surface area (and interaction diameter) of each ice element. Land points are shown by black circles.

Figure 4.   Positions of ice elements at time t=0, 300, 600, 900 days for the simulation. The size of the dots shows the surface area (and interaction diameter) of each ice element. Bonds between ice elements are plotted in magenta. Three tabular icebergs are shown, with 25, 16 and 4 elements respectively. Land points are shown by black circles.
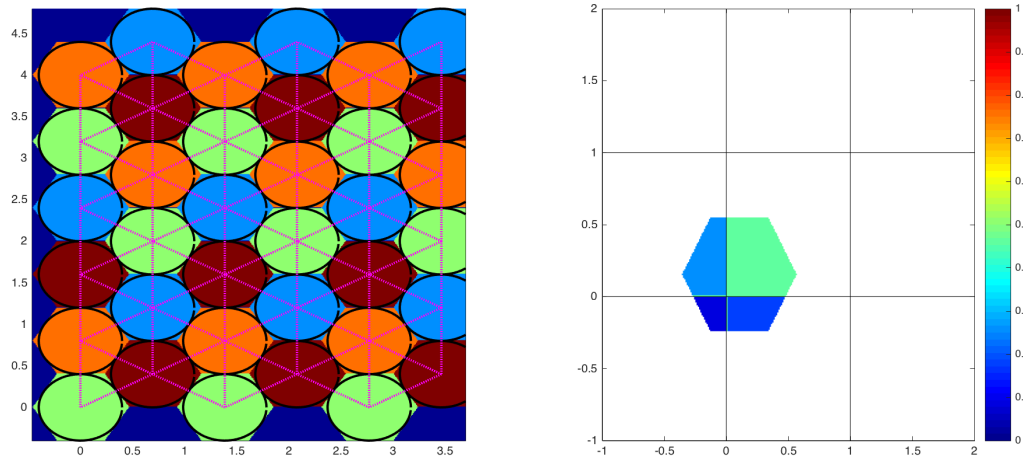
Figure 5. (a) Intersection of hexagonal element and ocean grid is used to find weights to spread LIISM properties to the ocean grid. (b) Hexagonal elements are initialized in a staggered lattice as shown. Adjacent elements are bonded together. The centers of bonded elements are plotted in pink. The element bonds form equilateral triangles which give the larger structure rigidity. The black circles shows to the interactive length scales used in element interactions.
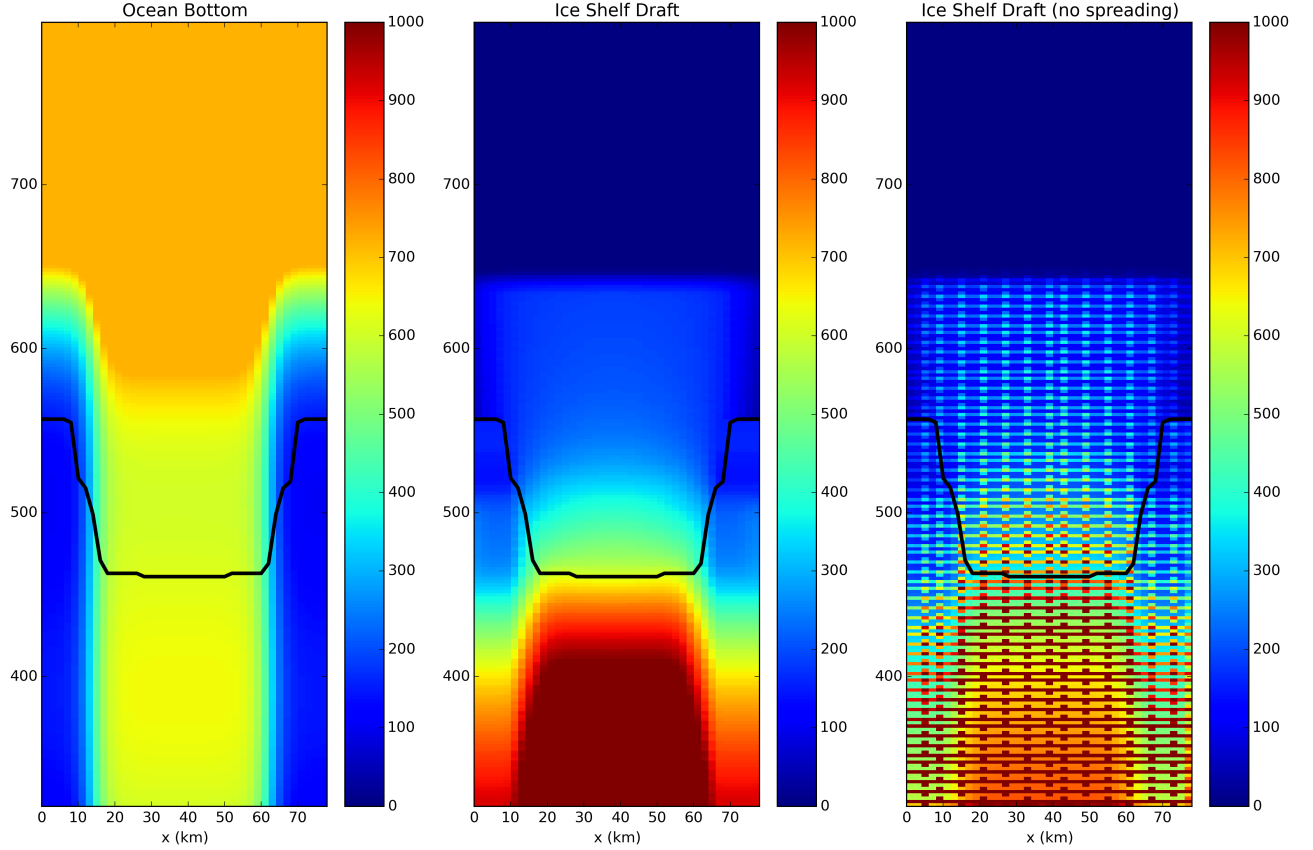
Figure 6. (a) Ocean bottom topography in ISOMIP configuration. (b) Ice shelf draft used in static shelf experiment. The ice draft is calculated from the ice mass in an ocean grid cell, which is found by spreading ice mass across ocean cells accounting for the size of each element (as explained in Section ?). (c) Same as in panel (b), except that the interpolation does not account for iceberg size, and instead treats elements as point masses.
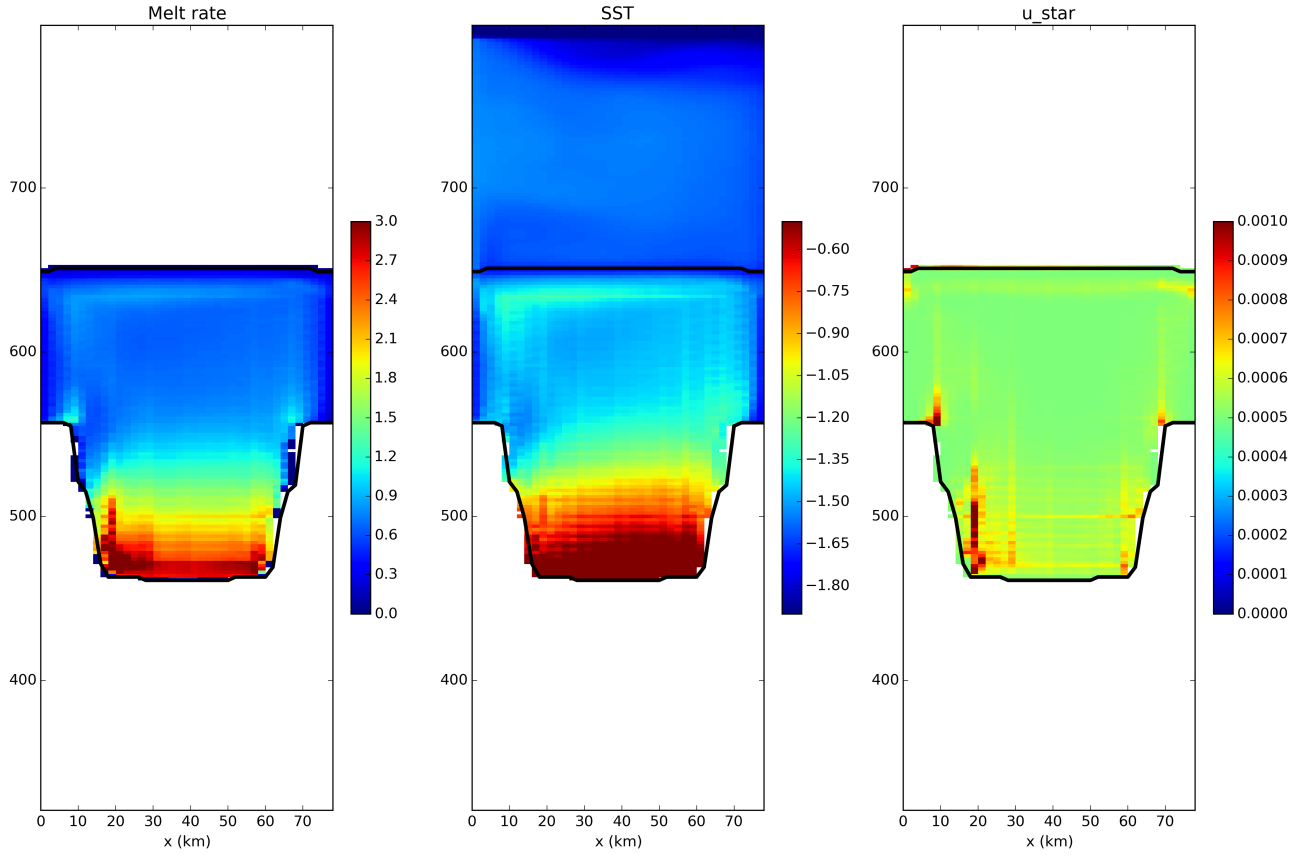
Figure 7. Results of the static ice shelf experiment using the LIISM model. The three panels show 5 year time average of the (a) melt rate, (b) ocean surface temperature and (c) u^* in the top layer of the simulation (at the surface or directly below the ice shelf).
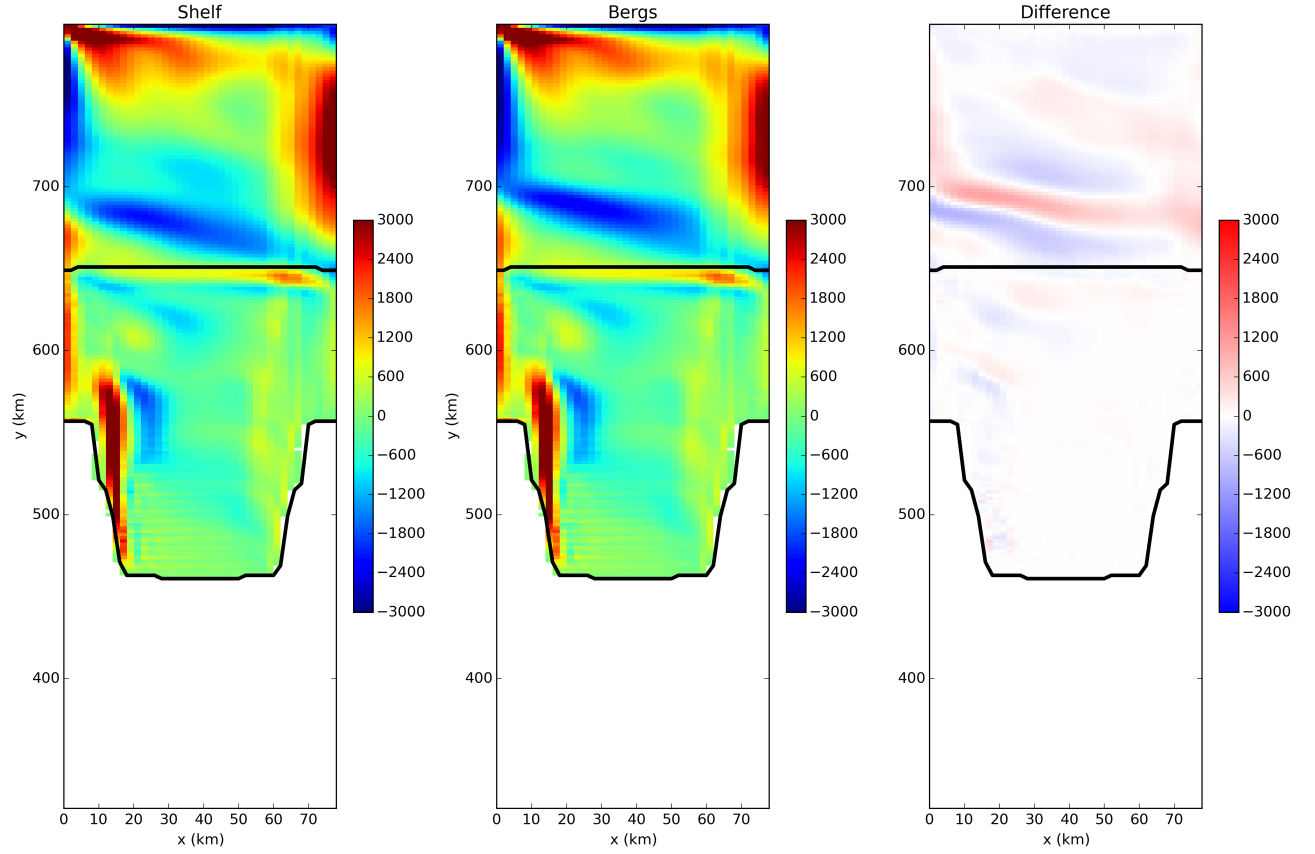
Figure 8. Comparison of Eulerian ice shelf model and Lagrangian Ice shelf model barotropic stream function
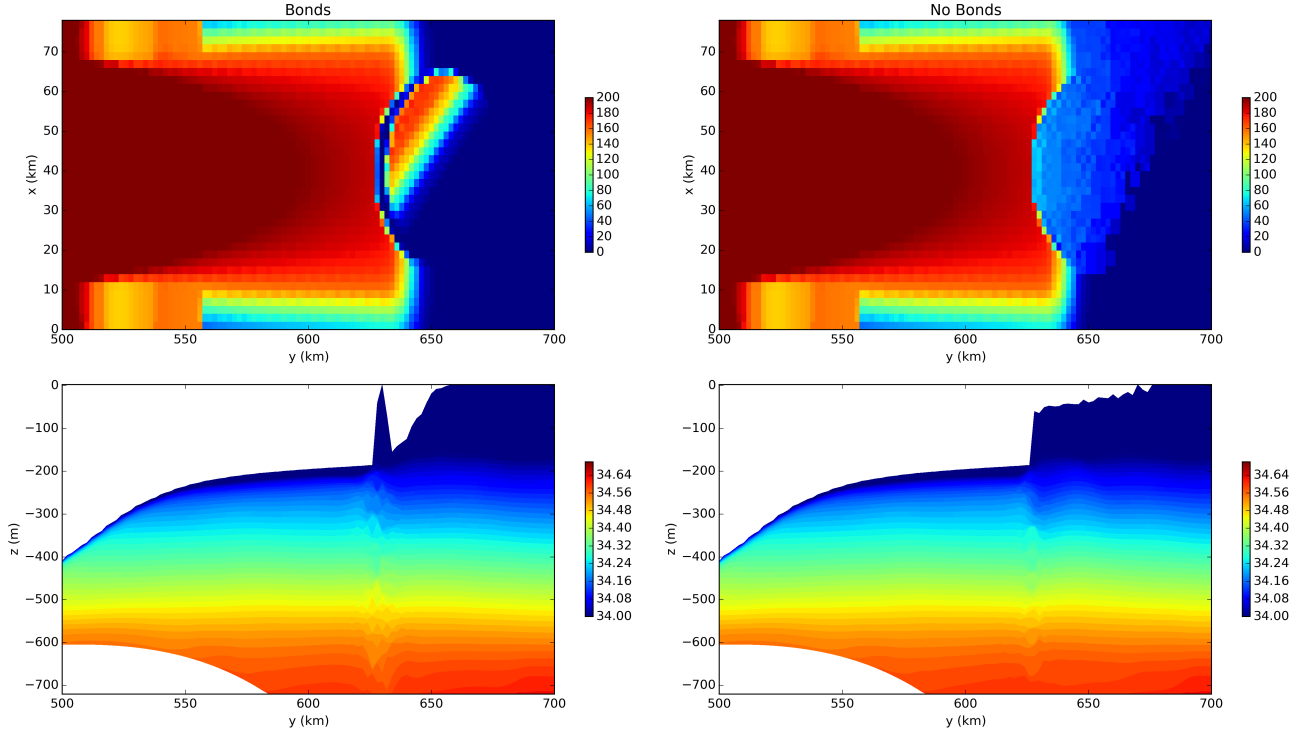
Figure 9.   Calving of tabular iceberg with the LIISM model fully coupled to the ocean for simulations with and without bonds between ice elements. The top row show the aveage draft of ice above the ocean in each grid cell for the simulation (a) with and (b) without bonds. The bottom row shows the corresponding temperature section at $y = \frac{L_y}{2}$ for the simulation (a) with and (b) without bonds. All snapshots are taken at time t= 30 days.
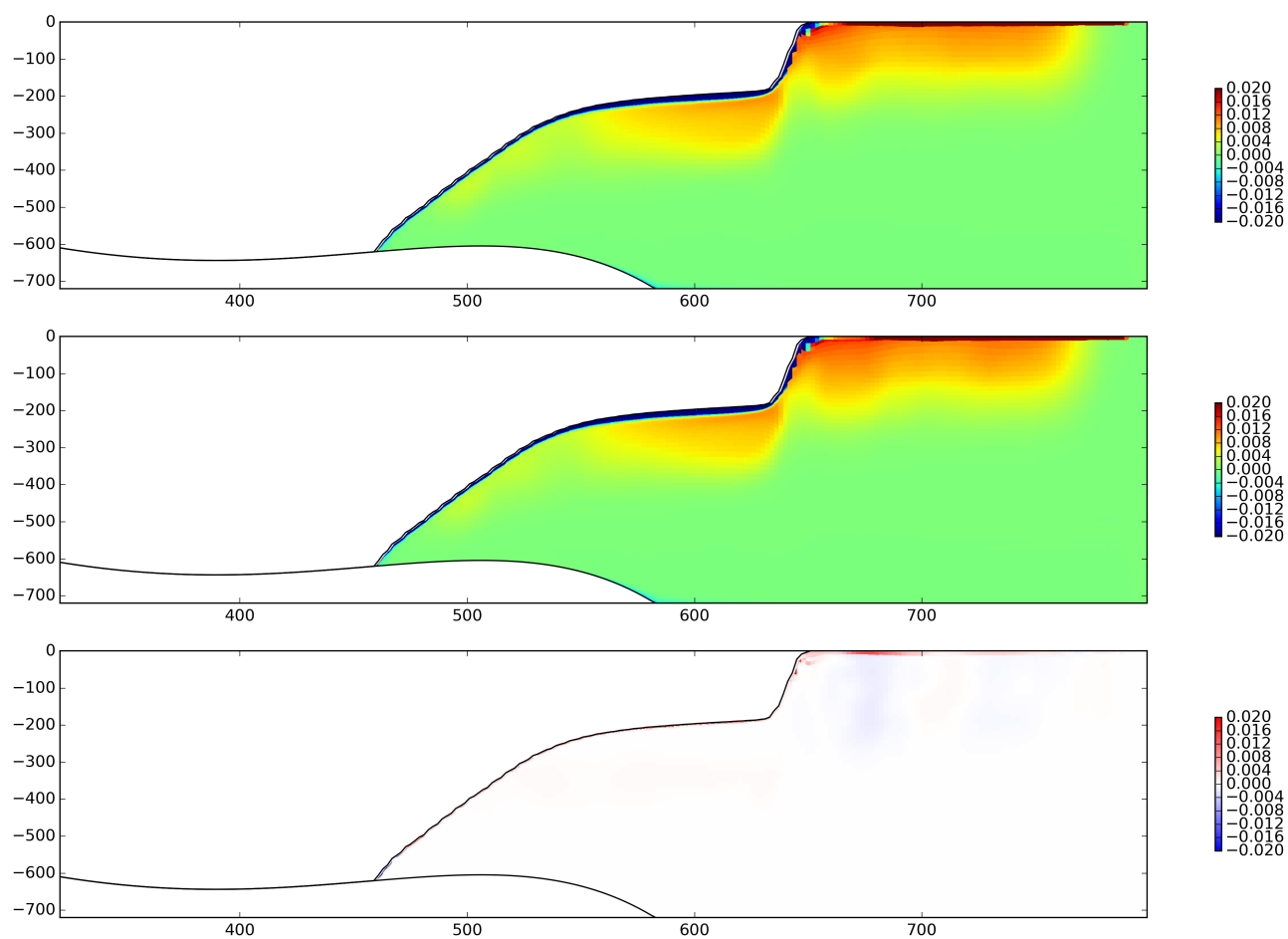
10. Supplementary Figures

Figure S1.   Comparison of Eulerian ice shelf model and Lagrangian Ice shelf model salinity fields.
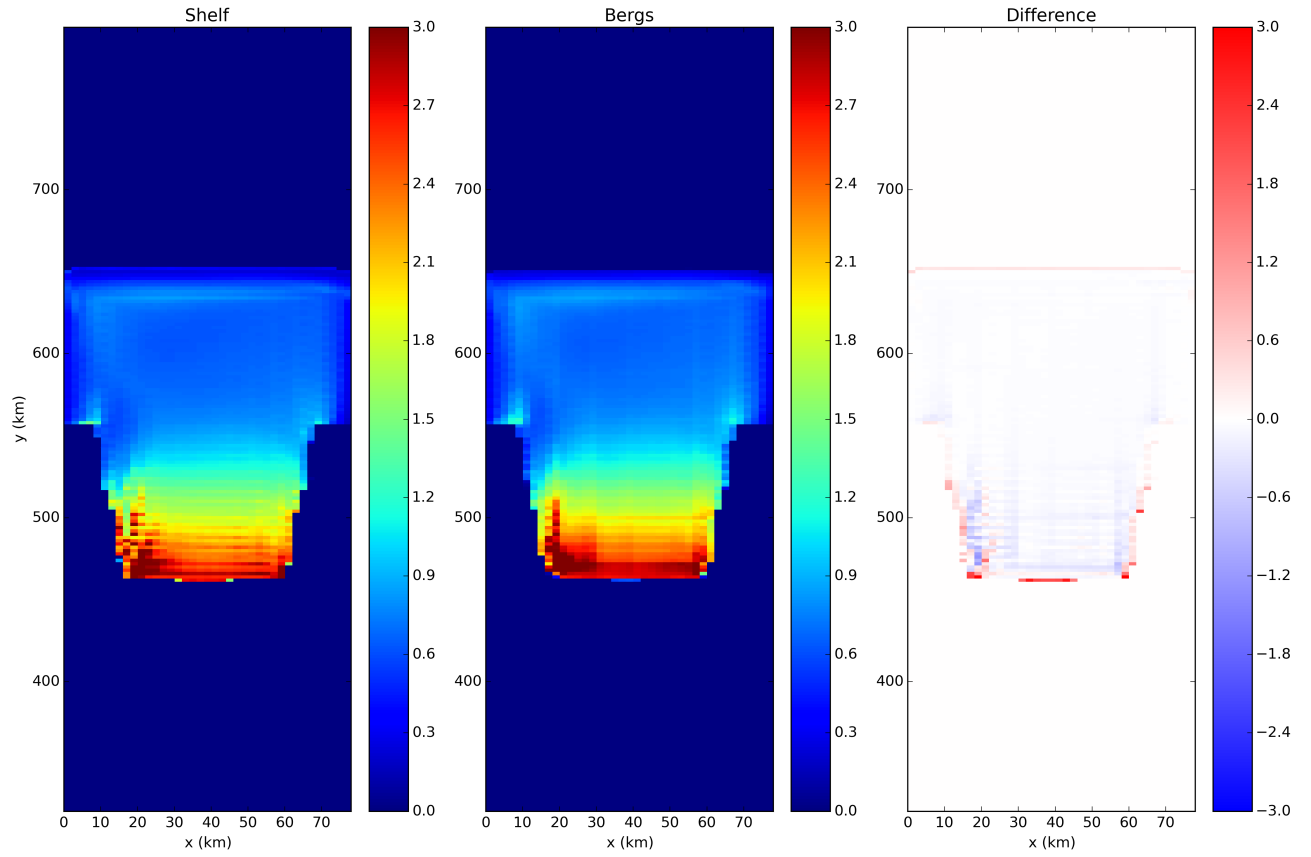
Figure S2. Comparison of Eulerian ice shelf model and Lagrangian Ice shelf model melt fields.
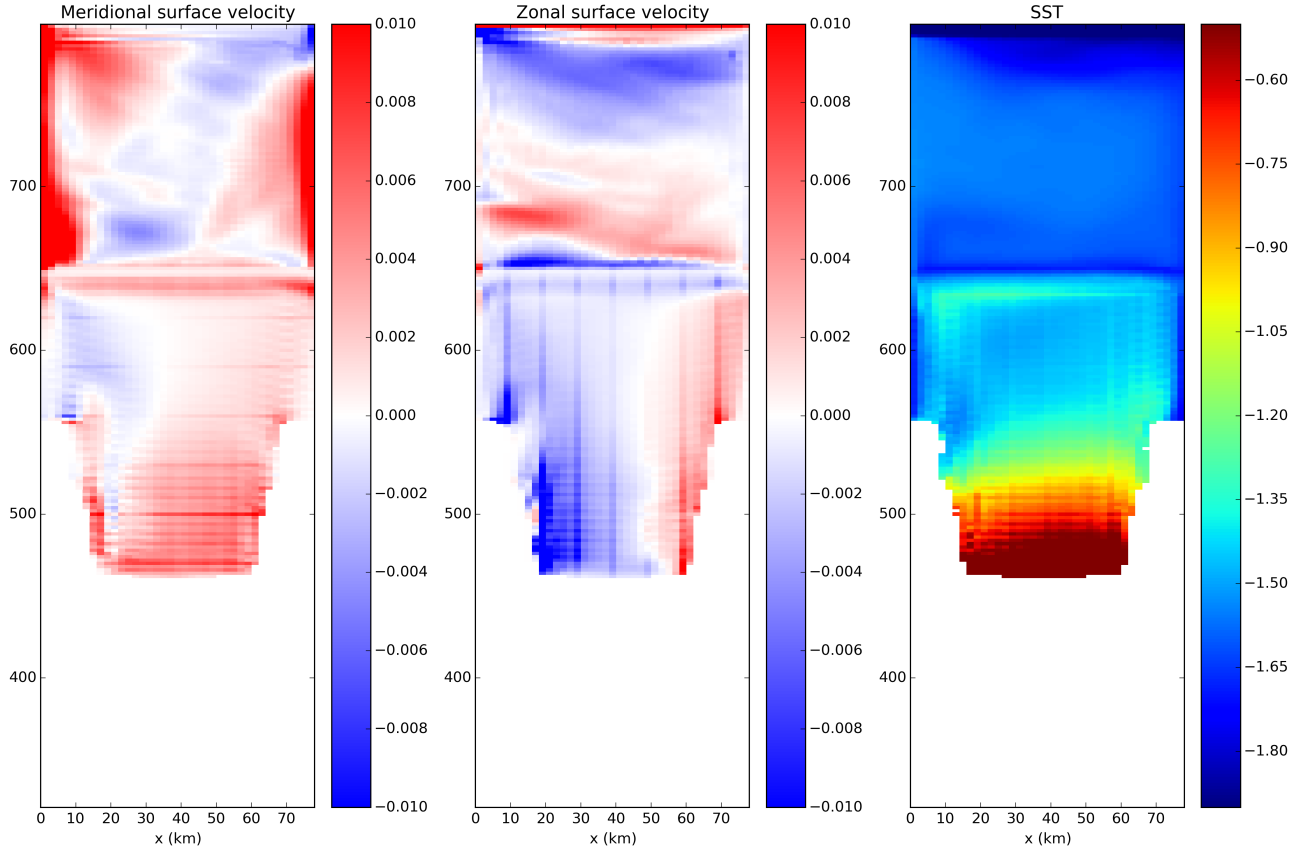
Figure S3.   Results of the static ice shelf experiment using the LIISM model. The three panels show 5 year time average of the (a) meridional velocity, (b) zonal velocity and (c) ocean temperature in the top layer of the simulation (at the surface or directly below the ice shelf).